Norwegian University of
Science and Technology

Quantitative (S)TEM analysis of intermediate band solar cell materials

Magnus Kristofer Nord

Master of Science in Physics and Mathematics

Submission date:	June 2011
Supervisor:	Randi Holmestad, IFY
Co-supervisor:	Turid Reenaas, IFY
	Per Erik Vullum, SINTEF

Norwegian University of Science and Technology
Department of Physics

Preface

The work on this thesis was performed between January and July 2011 as the conclusion of my studies to the degree Master in technology at the Norwegian University of Science and Technology (NTNU). The work was carried out at the TEM group at the Department of Physics.

I would like to thank my supervisor Randi Holmestad, and my co-supervisors Per-Erik Vullum and Turid Worren Reenaas for guidance and encouragement.

Particular thanks to Chris Boothroyd at the Technical University of Denmark for skillful operation of the electron microscopes used in this thesis. Finally I would like to thank Ruben Bjørge and Hanne Kauko for valuable information about multislice simulations.

Abstract

In this thesis the strain properties of two InAs/GaAs quantum dot intermediate band solar cell materials have been explored. Both samples were thin films grown on a (100) GaAs substrate. The quantum dot material was InAs, and the bulk material was GaAs. One sample had AlAs-cap, while the other had GaAs-cap. Geometrical phase analysis was used to study the strain. A higher degree of strain was found in the AlAs-capped sample. Negative strain was observed in directly above and below the quantum dots in both samples. A stacking fault in a quantum dot in the AlAs-capped sample was found to relax all the strain.

Analysis of the chemical composition of the AlAs-capped sample was performed using HAADF-STEM and multislice analysis. This analysis found an average indium concentration inside the quantum dots of 25% $\pm$ 10%, with peaks up to 50%.

Contents

1 Introduction **1**
1.1 Motivation . . . 2
1.2 Thesis structure . . . 3
1.3 Notation and abbreviations . . . 3

2 Theory **5**
2.1 Solar cells . . . 5
2.1.1 Basics . . . 5
2.1.2 The intermediate band . . . 8
2.2 Materials . . . 1
2.2.1 Strain in lattice mismatched epitaxy . . . 2
2.3 Molecular Beam Epitaxy . . . 3
2.4 Transmission Electron Microscopy . . . 4
2.4.1 Electron interactions . . . 4
2.4.2 The Transmission Electron Microscope . . . 5
2.4.3 Electron optics . . . 6
2.4.4 Image contrast . . . 8
2.4.5 High-Resolution Transmission Electron Microscopy . . . 9
2.4.6 Scanning Transmission Electron Microscopy . . . 10
2.4.7 Aberration correction . . . 13
2.4.8 Electron Energy Loss Spectroscopy . . . 14
2.5 Geometrical phase analysis . . . 14
2.6 Multislice simulations . . . 17
2.6.1 Some background on simulations . . . 17
2.6.2 The multislice method . . . 17
2.6.3 Frozen-phonon method . . . 19

3 Method and experiment **21**
3.1 Samples . . . 21
3.2 Sample preparation . . . 23
3.3 Experimental equipment . . . 26

3.4 Geometrical Phase Analysis . . . 26
3.5 The multislice simulations . . . 28
3.5.1 Root-mean-square displacement . . . 28
3.5.2 Simulation input parameters . . . 28
3.5.3 Element mixing . . . 30
3.5.4 Probe scanning position . . . 31

4 Results **33**
4.1 Strain mapping . . . 33
4.1.1 Strain direction . . . 33
4.1.2 Sample comparison . . . 33
4.1.3 Stacking faults . . . 36
4.1.4 Reciprocal-space analysis . . . 41
4.2 Multislice simulations . . . 42

5 Discussion **49**
5.1 Strain analysis . . . 49
5.1.1 Strain direction . . . 49
5.1.2 GaAs-capped vs. AlAs-capped . . . 49
5.1.3 Strain relaxation through stacking fault . . . 50
5.2 Multislice simulations . . . 51

6 Conclusion **53**

7 Further work **55**

References **55**

A Indium concentration, error estimate **63**

Nomenclature

ADF	Annular Dark-Field
AlAs	Aluminum arsenide
CB	Conduction Band
CPU	Central processing unit
EELS	Electron Energy Loss Spectroscopy
GaAs	Gallium arsenide
GPA	Geometrical Phase Analysis
GPU	Graphics processing unit
HAADF	High-Angle Annular Dark-Field
HRTEM	High-Resolution Transmission Electron Microscopy/Microscope
IB	Intermediate Band
IBSC	Intermediate Band Solar Cell
InAs	Indium Arsenide
LAADF	Low-Angle Annular Dark Field
MBE	Molecular Beam Epitaxy
QD	Quantum Dot
S-K	Stranski-Krastanov
STEM	Scanning Transmission Electron Microscopy/Microscope
TEM	Transmission Electron Microscopy/Microscope

TJ	tera joule
VB	Valence Band
VLM	Visible Light Microscope

Chapter 1

Introduction

Demand for energy is increasing every year[1]. The primary cause for this rapidly increasing demand is two-fold: a growing world population and increasing living standards. Production of energy must increase to keep up with this demand. Fossil fuels are the most readily available energy source: coal, oil and gas. About 80% of world wide energy production is based on these fossil fuels. All fossil fuels release greenhouse gases like CO_2 when consumed, and these gases are one of the leading sources of anthropogenic global climate change. Limiting the release of climate gases is thus instrumental in avoiding radical climate changes, however the increasing energy demands must somehow be met. Another aspect is the finite nature of these fuel sources: in a long-term perspective they will simply run out.

Another factor fueling the development of alternative energy sources is energy independency. A nation's ability to supply energy to its industry and population is vital. Thus having a secure and predictable energy source is vital for national security. Currently the majority of nations rely on imported fossil fuels. This makes them dependent on the will of the nations supplying the fossil fuels. Not having this dependency is vital[2]. Alternative energy sources allow states to produce their energy within their own borders, making the supply much more secure.

Issues with fossil fuel sources has lead to an increased interest in environmentally sustainable energy sources: so-called alternative energy. This increased interest has lead to rapid development of technologies related to different clean renewable energy sources.

One of these energy sources is solar power. Calculating the potential for solar power is fairly straightforward: every second 162000 terajoule (TJ) of sunlight hit the Earth, of which about 5000 TJ is reflected back into space[3]. Human civilization consumes on average 16.6 TJ energy every second[1]. Collecting about 0.33% of the reflected sunlight would cover the whole world's energy needs, therefore the potential for solar energy is enormous.

1.1 Motivation

The efficiency η of a solar cell is a measure of how much of the incident photon energy it can convert to electricity and is given by,

$$\eta = \frac{E_{\text{electricity}}}{E_{\text{incident light}}}, \tag{1.1}$$

where $E_{\text{electricity}}$ is the electrical output from the solar cell and $E_{\text{incident light}}$ is the energy of the light hitting the solar cell. Given two solar cells where one of them has twice the efficiency of the other, the more efficient solar cell would only require half the area while still producing the same amount of energy. Using less area is highly beneficial, since it is usually both costly and limited.

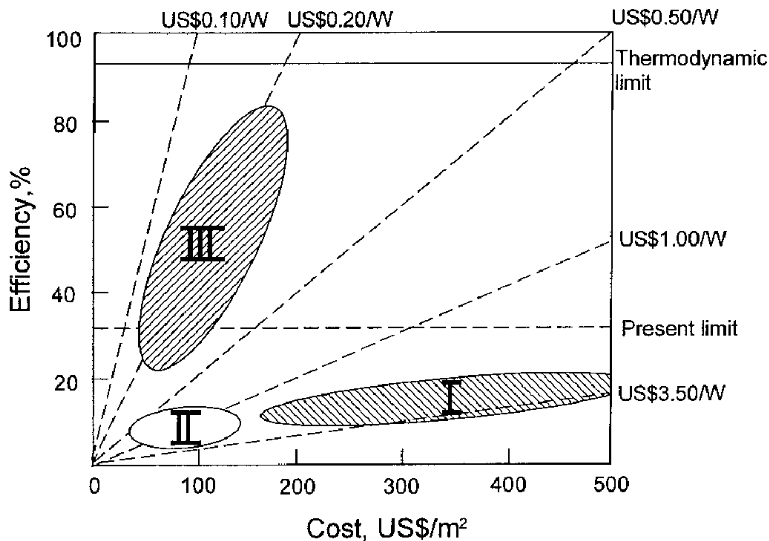

Figure 1.1: Efficiency and cost projections for first, second and third generation solar cells. Figure from Green[4].

The most common type of solar cell is based on silicon wafers, so-called first generation solar cells. These silicon based solar cells have a theoretical maximum efficiency of about 30%[5], but most commercial solar cells of this type have an efficiency of about 15%. As production methods have matured the price of these devices has fallen greatly, making most of price tied to the material costs[6]. This has prompted the development of thin film based solar cells, so-called second generation solar cells. Such cells use substantially less materials and have the potential to be much cheaper. One downside for both first and second generation solar cells is the low efficiency limit of about 30%. Many new types of solar cell designs, often called third generation solar cells, are being developed to beat this 30% limit. Cost and efficiency projections for the different solar cell generations can be seen in fig. 1.1.

The intermediate band solar cell studied in this thesis is a third generation solar cell design, and is theoretically able to beat the 30% limit by utilizing more of the sunlight.

1.2 Thesis structure

This thesis is organized in the following fashion:

Chapter 2, **Theory**. First the theoretical background of the solar cell will be discussed. This include how a solar cell works, how the energy production of a solar cell is limited by efficiency lossesand different ways to overcome this limit. This is followed by a introduction to the intermediate band (IB) solar cell: IB as a solution to the efficiency limit and how to make an IB work. Then an overview of the different material components in the solar cell material will be given, and the method used to make the material: Molecular Beam Epitaxy using the Stranski-Krastanov growth mode. Next several different subjects related to the Transmission Electron Microscope (TEM) are discussed: the basics of eletron-matter interactions, the basics on how a TEM works, Scanning Transmission Electron Microscopy (STEM) and High-Resolution Transmission Electron Microscopy (HRTEM). Last two analytical methods for analysing the experimental results are explained: Geometrical Phase Analysis (GPA) and multislice simulation.

Chapter 3, **Method and experiment**. This chapter gives an overview of the parameters used in the production of the solar cell samples and information about the experimental equipment which was used. In addition the sample preparation techniques and the different parameters used in the GPA and multislice simulations will be discussed.

Chapter 4, **Results**. First an overview of the two samples is given, which is followed by a presentation of the results from the GPA and from the multislice simulations.

Chapter 5, **Discussion**. Different features obtained from the GPA will be discussed, including the differences between the two samples. In addition the multislice results for the AlAs-capped sample will be discussed..

Some notes about the thesis itself: A basic knowledge about solid-state physics is assumed: diffraction, band theory, Fermi levels, some basic quantum mechanics, stacking faults and zone axes.

1.3 Notation and abbreviations

As noted in the list of abbrevations, TEM can mean either Transmission Electron Microscopy, which is the technique or method, or Transmission Electron Microscope, which is the device or instrument. Sometimes “TEM images” will refer to images that can be taken on a Transmission Electron Microscope, which includes both “regular” TEM and STEM. In other cases TEM will specifically refer to “regular” TEM. It should be clear from context which one is being referred to.

Standard TEM notation will be used for denoting different vectors.

- Specific zone axes will be denoted by $[\cdot]$, e.g. [100].
- $\{\cdot\}$ will denote a specific Bragg reflection, e.g. $\{111\}$.
- $<\cdot>$ will denote a general direction, e.g. $\langle 220 \rangle$.

Chapter 2

Theory

This chapter discusses the various techniques and concepts needed to understand the experiment and results in this thesis. The chapter will cover four major subject areas. Solar cells in general and the intermediate band solar cell. The materials used to create the intermediate band solar cell materials and the molecular beam epitaxy which was used to manufacture them. The basics of Transmission Electron Microscopy will be discussed, including STEM and HRTEM modes. An overview of the analysis methods: geometrical phase analysis and multislice simulations. If the reader has prior knowledge about these subjects, this chapter can be safely skipped.

2.1 Solar cells

2.1.1 Basics

A solar cell is a material which has the ability to convert photons directly to electricity. This conversion is achieved by using the photovoltaic effect: a photon excites an electron from one band to another, for example from the valence band (VB) to the conduction band (CB) as shown in fig. 2.1c. The process from photon to electric current can be seen in fig. 2.1a. An electron is placed in the conduction band, while an electron-hole is created in the valence band. The electron-hole (often simply called a hole) has similar properties as the electron, and can be viewed as a particle in the context of solar cells. An electron and a hole is simple called an electron-hole pair. This electron-hole pair is then extracted from the solar cell, and an electric current is created. The voltage produced by the solar cell will be a function of the energy difference between the VB and CB, which will be referred to as the bandgap. Photons with energy *less* than the bandgap will be refered to as below-bandgap photons. Photons with energy *more* or equal to the bandgap will be refered to as above-bandgap photons.

The device presented in the previous paragraph is a single band solar cell, which has a maximal theoretical efficiency of about 30%. Ideally this number should be

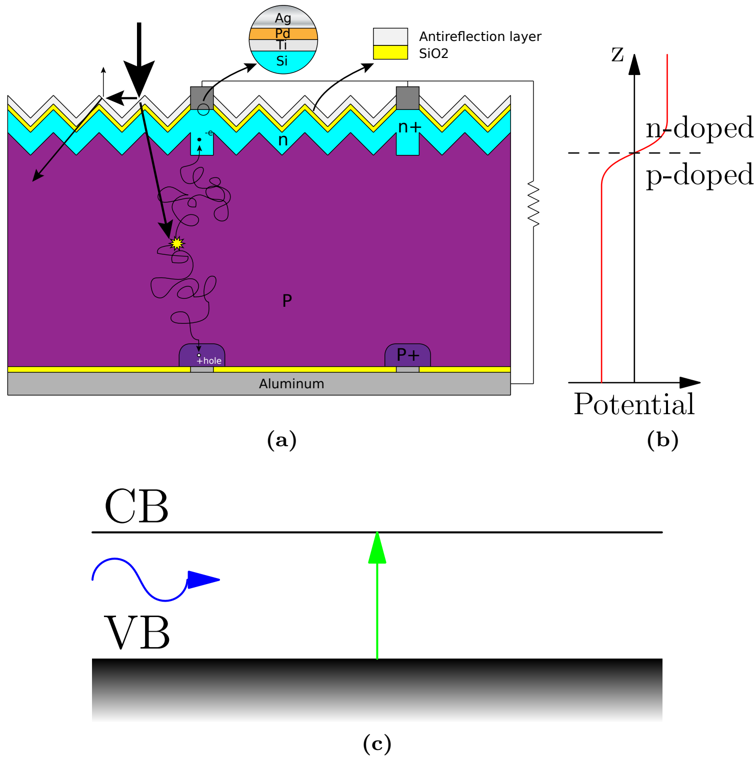

Figure 2.1: (a) Schematic of a single band silicon solar cell. The arrows show two possible paths for a photon: transmission into the solar cell and reflection away from the solar cell. The antireflection layer serves two functions: maximizing the amount of photons transmitted into the solar cell and reduce the amount of electron-hole recombinations at the surface. An electron-hole pair is created when a photon impacts somewhere in the doped silicon area. Then the potential profile of the solar cell shown in (b) leads the electron to the n-doped silicon while the hole is lead to the p-doped silicon. Lastly the electron is extracted by the gray silver contacts and the hole is extracted by the bottom aluminum contact. Image from Wiki Commons[7]. (b) Shows the potential profile of the solar cell depicted in (a). (c) Bandgap in a single band solar cell like the one shown in (a): the blue arrow represents a photon which excites an electron from the valence band to the conduction band (green arrow), creating an electron-hole pair.

100%, but there are several processes which lead to energy being lost:

- Photons with energy lower than the bandgap will not be absorbed, thus not creating any electron-hole pairs in the solar cell.
- Photons with energy *higher* than the bandgap will create an electron-hole pair. The electron-hole pair will relax down to the bandgap energy by releasing energy through phonons.
- Electron-hole pairs can recombine over the bandgap, creating a photon with energy equal to the bandgap.
- Electron-hole pairs can recombine over the bandgap, without creating a photon. This is caused by some electronic state in the bandgap which is often supplied by a dislocation or impurity in the solar cell material.

All these processes are shown in fig. 2.2.

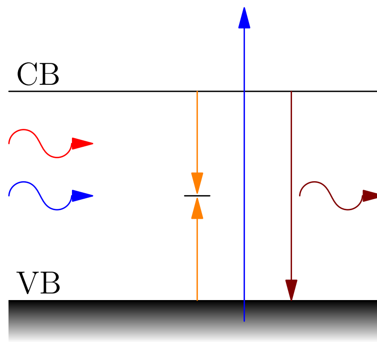

Figure 2.2: Different processes which lead to efficiency losses. Blue arrow: photon with energy greater than the bandgap of the solar cell. The electron-hole pair created by the photon will relax down to the bandgap through phonons. Red arrow: photon with energy less than the bandgap will not excite any electron-hole pairs, thus they will not contribute to production of an electrical current. Orange arrows: electron-hole pair recombining through some electronic state in the bandgap. Brown arrow: electron-hole pair recombining over the bandgap, releasing a photon in the process.

Radiative recombinations will usually not lead to a large efficiency loss, since the photons created in this process can be absorbed later. Non-radiative recombinations are most commonly caused by impurities inside the solar cell, an issue which can be alleviated through higher quality materials or better production methods.

There are two additional sources of efficiency loss: the below- and above-bandgap photons. They can not be easily fixed because they are an intrinsic part of the single band solar cell. By assuming the efficiency losses from raditative and non-radiative losses can be completly removed, it is possible to calculate the maximum possible efficiency of a single band solar cell. By using the solar spectrum

which passes through the atmosphere as a basis, it is possible to calculate the efficiency for different bandgap sizes. This calculation gives a theoretical maximum efficiency for a single band solar cell of about 30%[8]. This theoretical maximal efficiency is centered on a bandgap of 1.1 eV, which is the bandgap of silicon. One important factor is the amount of light which is incident on the solar cell. By using lenses or mirrors it is possible to greatly increase the energy production. Assuming similar conditions as earlier and maximal concentration of light, the efficiency increases to 40.7%. To go beyond this efficiency limit, something must be done with either the below- or above-bandgap photons. Solar cell designs which attempt this are usually referred to as third generation solar cells.

One possibilty is combining several single band cells with different bandgaps. Placing the solar cell with the largest bandgap on top allows the high energy photons to be absorbed, while the remaining lower-energy photons will pass through it. These lower energy photons will then be absorbed by a solar cell with lower bandgap further down. Thus a greater amount of the light will be utilized. This design is called a multi-junction cell, and is currently the most successful third generation solar cell. There are two ways of achieving this arrangement: growing (see section 2.3 for growing thin films) solar cell material on top of each other, or growing them separately and connecting them afterwards. The former is potentially the cheapest method, however large lattice mismatching causes dislocations to form. The latter avoids this problem, but is highly expensive since each solar cell piece requires its own circuitry[6]. The high cost has kept it out of commercial use, except in the space industry where the high efficiency has made it especially popular for use in spacecrafts.

Another design is the multiple excitation generation (MEG) solar cell. An electron-hole pair with more energy than the bandgap, will usually relax down to the bandgap. If the energy of the electron-hole pair is greater than twice the bandgap, it can create additional electron-hole pairs[9]. This process is very rare in regular solar cells and does not contribute much to the efficiency, but if the phonon assisted relaxations could be suppressed the probability of MEG increases[10]. A single band solar cell with MEG can reach a theoretical efficiency of 44.4%[11].

2.1.2 The intermediate band

Another interesting concept is the intermediate band solar cell, which is the focus of this thesis. An intermediate band (IB) is introduced between the CB and the VB. This new band allows two additional electron-hole excitations: from the VB to the IB and from the IB to the CB, both shown in fig. 2.3. Utilization of the below-bandgap photons is thus possible, which allows the optimal values for VB-CB bandgap to be increased. This increase in the VB-CB bandgap allows utilization of a larger part of the above-bandgap photons. By using the same assumptions as earlier, ignoring non-radiative and radiative efficiency losses, an efficiency value of 63.2% is calculated. This value assumes maximal light concentration, and the following values for the different bandgaps: VB to IB 1.24 eV; IB to CB 0.71 eV; 1.95 eV between the CB and VB[12].

One way of creating an IB is by introducing a narrow density of states some-

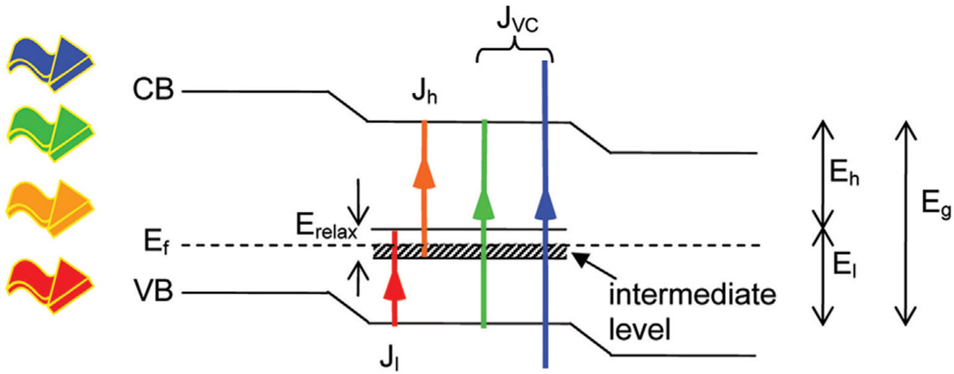

Figure 2.3: Different ways electron-hole pairs can be created in an IB solar cell (IBSC). Below-bandgap photons (red and orange) can excite electrons from the VB to the IB, or from the IB to the CB. Above-bandgap photons (green and blue) will excite electrons from the VB to the CB. Both these processes will run in parallel. Figure from Conibeer[13].

where between the CB and the VB. This can be achieved by using quantum dots (QDs)[14].

QDs[1] are semiconductors where the electrons are confined in all three spatial dimensions[15]. This enables the QD's electron states to have clearly defined energy levels, caused by quantum confinement. "Tailor-making" of the energy-levels in the QD is thus possible, by varying the size of the QDs[16]. If the QDs are placed sufficiently close to each other, the energy levels will overlap. These overlapping energy levels will create mini-bands which act as an IB. The mini-bands create 3 quasi-Fermi levels: E_{FI}, E_{FC} and E_{FV}[17] at the IB, CB and VB respectively. This is shown in fig. 2.4a.

If the IB is going to contribute to the electric current of an IBSC, then electrons must be able to pass all the way from the CB to the VB via the IB. Exitation from the VB to the IB will occur frequently, but the IB to CB transition is a bit more tricky: the IB must be half-filled with electrons. The IB is half-filled by growing the QDs in an undoped material, then sandwiching it in between a p- and n-doped material. This arrangement is show in fig. 2.5. The sandwiching will create a flatband potential over the QDs, which will allow the IB to be half-filled as shown in fig. 2.4b.

Introduction of electronic states in the middle of the bandgap can lead to non-radiative recombinations. The QDs should therefore reduce the amount of electron-holes extracted from the solar cell[18]. However this behavior is suppressed if the the energy levels of the QDs are overlapping. Creating an IB which increases the efficiency of a solar cell will therefore requires both evenly spaced and similarly sized QDs[19].

Fulfilling both requirements of evenly spaced and similarly sized QDs creates a solar cell generating electron-hole pairs from the CB to VB bandgap, and a parallel

[1] Sometimes referred to as nanocrystals

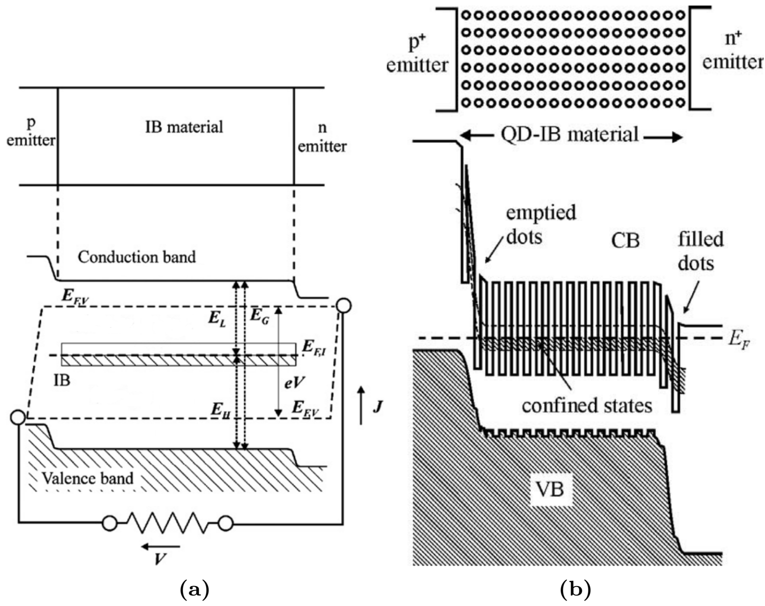

Figure 2.4: (a) Shows three different features: the quasi-Fermi levels E_{FI}, E_{FC} and E_{FV}; the flatband potential in the area of the IB material; the energy levels between the different bands. (b) Similar to figure (a), but showing how the electron states of the QDs is filled in the flatband potential. Both figures from Martí et al. [12]

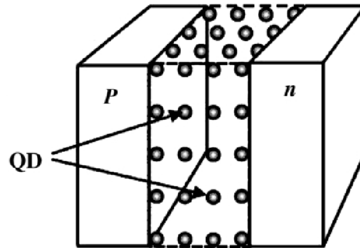

Figure 2.5: Real space representation of quantum dots (QDs) placed periodically in a semiconductor, creating an intermediate band. The semiconductor with the QDs is sandwiched between a p- and n-doped semiconductor material. Figure from Cuadra et al.[20].

Table 2.1: Overview of the lattice parameter and bandgap for the compounds relevant to this project

Compound	Lattice parameter [Å]	Bandgap [eV]
GaAs	5.6533[24]	1.424[25]
AlAs	5.6605[24]	2.12[26]
InAs	6.0583[22]	0.354[27]

process generating electron-hole pairs via the IB. Individual QDs do not absorb a lot of light, necessitating a large number of them[21] to achieve a large increase in efficiency. The method of producing the IBSC materials can lead to the formation of dislocations and stacking faults which *lower* the efficiency: more layers of QDs cause more structural damage, which results in lower efficiency. Thus more layers of QDs have been correlated with lower efficiency: a solar cell with 10 QD layers achieved higher efficiency than one with 20 QD layers[22]. A different production method which does not introduce defects is needed. For more information about the IB, see Martí and Luque[23].

2.2 Materials

There are three key materials in this project: gallium arsenide (GaAs) a compound consisting of gallium and arsenic; aluminum arsenide (AlAs) a compound consisting of aluminum and arsenic; indium arsenide (InAs) a compound consisting of indium and arsenic.

GaAs has a crystal structure consisting of two face-centered cubic sublattices, with the second cube shifted by 1/4 of a cube's diagonal with respect to the first cube. One of the FCC lattices consist of gallium, while the other consist of arsenic[24]. InAs is similar: the FCC with Ga is replaced by a FCC with In. AlAs is also similar to GaAs but Al replace Ga.

Indium, gallium and aluminum all have three electrons in their outer energy levels, which makes them a part of the III group in the periodic table. Therefore they share many chemical properties, including the ability to bond to arsenic. Arsenic has five electrons in its outer energy level, making it a part of the V group in the periodic table. The compound of a group III and V element, which also is a semiconductor, is commonly called a III/V semiconductor. The similar properties of GaAs, InAs and AlAs cause them to have the same zincblende structure which can be seen in fig. 2.6.

The important lattice parameter and bandgaps for the materials discussed can be seen in table 2.1.

There is a 7% difference in the size of the InAs and the GaAs unit cell. The difference between the size of the unit cell of AlAs og GaAs is about 0.1%. The latter difference will be negligible, while the former is quite large and will introduce strain in an epitaxial crystal system.

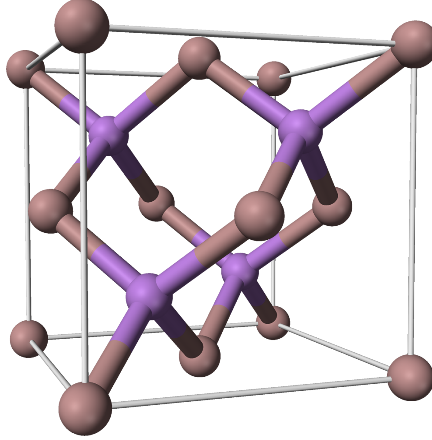

Figure 2.6: The zincblende structure. For GaAs: one FCC lattice of Ga, one FCC lattice shifted by (1/4,1/4,1/4) times the lattice parameter of the first FCC consisting of As. For AlAs: Al replaces the Ga at in the first FCC structure. InAs: In replace Ga in the first FCC lattice.

2.2.1 Strain in lattice mismatched epitaxy

Strain is a rather broad subject and can take many forms. This section will briefly discuss what happens when one gets lattice mismatch in an epitaxial system.

Figure 2.7 shows the effects of a layer with larger unit cells being grown on a smaller bulk. The unit cells will expand in the growth direction (y-direction in fig. 2.7), and compress in the x-direction. The unit cells in the new layer will match the bulk unit cells in the x-direction. The amount of expansion in the y-direction is estimated by the formula[28, p. 227],

$$\varepsilon_{xx} = \frac{a_S}{a_L} - 1 \tag{2.1}$$

$$\varepsilon_{yy} = \frac{\varepsilon_{xx}}{\sigma} \tag{2.2}$$

$\varepsilon_{xx}$is the amount of compression for the new layer's unit cells in the x-direction. ε_{yy} is the same, but for the y-direction. a_S is the lattice constant for the bulk substrate. a_L is the lattice constant for the new layer. σ is the Poisson ratio, which is a material constant. ε_{yy} for InAs grown on a GaAs substrate is 0.19, by using eqs. (2.1) and (2.2). These formulas are only valid within certain limits. At a certain point the system will create stacking faults or dislocations, instead of expanding in one direction and compressing in another. This only occured once in the samples examined in this thesis.

The difference in unit cell size between GaAs and AlAs is negligible, thus no seperate calculations were done for AlAs.

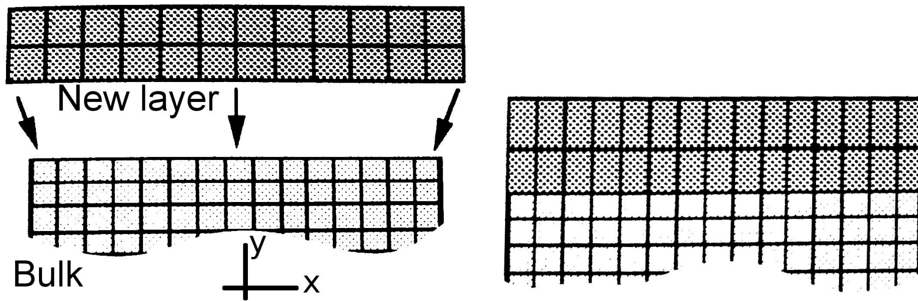

Figure 2.7: The effect of growing a layer which has a larger unit cell size compared to the bulk. The unit cells in the new layer will compress to match the bulk lattice in the x-direction, and expand in the y-direction. Image from [28].

2.3 Molecular Beam Epitaxy

Molecular Beam Epitaxy (MBE) is a technique for growing thin films on substrates. The thin films are grown by having the substrate in high vacuum, and subjecting it to a stream of atoms of the materials which the film should consist of. The substrate is kept at a high temperature (480 °C for GaAs), which causes the deposited material to diffuse on the surface. Several different structures can form on the surface of the substrate: a 2-dimensional (2D) layer, a 3-dimensional (3D) structures ("islands") or a mix of both. The latter is called the Stranski-Krastanov growth mode and can be used in the production of QD materials.

The S-K growth mode works by depositing two materials with a lattice mismatch, e.g. depositing InAs on GaAs. InAs has an approximatly 7% larger unit cell compared to GaAs, which will introduce strain in the system. Firstly the InAs will form a 2D layer, and the strain will accumulate as the layer becomes thicker. At a certain level of accumulated strain the InAs will self-assemble into a 3D structure, which is more energetically optimal for the system. This will create two different features: a 2D layer of InAs often called a *wetting layer*, and 3D structures called *quantum dots*[29, Chapter 6]. This structure is shown in fig. 2.8.

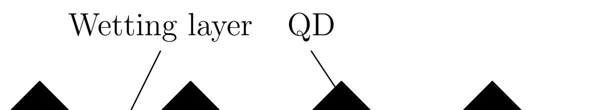

Figure 2.8: Schematic of the Stranski-Krastanov growth mode. The QDs are 3D structures which self-assemble when the strain in the layer accumulates above a certain value. The wetting layer is a 2D structure which "supplies" the material to the QDs.

The IBSC materials examined in this thesis were grown in a MBE, where the S-K growth mode was used for creating the QDs. Thomassen et al.[30] discovered an issue when when growing QDs in a similar fashion as described above. The QD

density and size was not homogeneous over the wafer. A likely culprit being the temperature variation over the wafer, caused by the position of the sample holders. Thus different parts of the wafer will have different growth conditions, which *may* cause different structures to be created. This is important to keep in mind, an analysis of one part of a wafer might give different results than another part of the sample.

For more information about MBE, see the book by Herman & Sitter[31]. For a thorough review of self-assembly QDs see the book *Self-assembled InGaAs/GaAs quantum dots*[32].

2.4 Transmission Electron Microscopy

This chapter will explain the different concepts related to transmission electron microscopy (TEM): the underlying physical phenomenon; some basic facts about TEM and how the optics in a TEM works; the differences between TEM and STEM mode; a discussion about the different sources of contrast which are vital in this thesis; a brief discussion on aberrations and how to correct them.

2.4.1 Electron interactions

There are numerous ways in which an electron can interact with a material. Knowing how these interactions work is essential in interpreting the different features observed in a TEM image. Only the interactions which are relevant for this thesis will be discussed. For a more thorough discussion of all the different interactions which can occur in a TEM, see the book *Transmission Electron Microscopy* by Williams and Carter[33].

In this chapter "the electron" or "electrons" will refer to a beam of electrons moving at a very high speed, not electrons which are bound to atoms.

When an electron moves through a material several things can happen:

1. It can go straight through the material without interacting with anything.
2. It can interact elastically
3. It can interact inelastically

Figure 2.9 show a schematic overview of the interactions. All these interactions will be discussed, as they are necessary for explaining the (S)TEM techniques used later.

The first interaction is commonly refered to as the direct beam, and is usually the strongest signal in a TEM. The direct beam is very dependant on the sample thickness. In thick samples all the electrons will interact, while in very thin samples almost all the electrons will go straight through the sample. To get good data from a TEM the sample must be sufficiently thin. The method for achieving this for the solar cell samples in this project is discussed in section 3.2.

The second interaction is based on an elastic interaction between an atom in the material and the electron. It is common to split the elastic interactions in

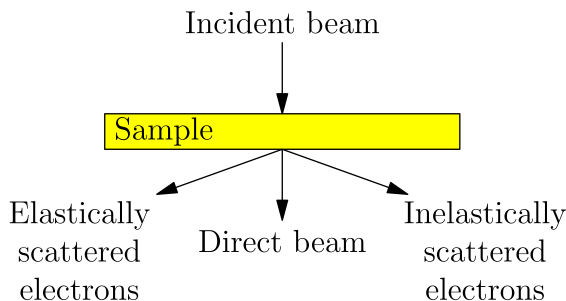

Figure 2.9: Some of the interactions which can happen when an electron interacts with a sufficiently thin sample. Note that the angles are highly exaggerated.

two different categories: coherent and incoherent scattering. The latter interaction is dominant at high scattering angles, and is primarily dependant on the atomic number of the scattering atom. These properties are heavily used in certain types of STEM, which will be discussed in section 2.4.6. Coherent scattering is the mechanicsm which forms diffraction patterns and is a major part of most TEM work. The coherency and wave nature of electrons leads to destructive and constructive interference. This is formalized in Bragg's law,

$$n\lambda = 2d \sin \theta_{\mathrm{b}}, \tag{2.3}$$

where λ is the wavelength of the beam, d is the distance between the atom planes, n in an integer and θ_{b} is the angle of the incident and the scattered beam. See fig. 2.10 for an overview of the geometrical variables.

A powerful formalism has been developed for explaining diffraction in crystal structures, however this is tangential to this project and has been omitted. More information about the phenomena can be found in *Introduction to Solid State Physics* by Charles Kittel[34](or any solid state physics book). The electron beams scattered in this fashion are usually much weaker than the direct beam.

2.4.2 The Transmission Electron Microscope

The human eye has a lateral resolution of about 200 µm. If we want to examine structures which are smaller, we need to use some kind of magnification. A familiar tool is the regular microscope which will be referred to as a visible light microscope (VLM). Using a VLM one can achieve a lateral resolution of about 200 nm. The limiting factor being the wavelength of light. The relationship between wavelength and lateral resolution R can be seen in Equation (2.4). The wavelength of the radiation is denoted by λ and NA is the numerical aperture:

$$R = \frac{0.61\lambda}{NA}. \tag{2.4}$$

In an ideal situation using blue light one gets 200 nm as mentioned earlier. An atom has a size of about an ångstrom making VLM unsuited for imaging structures

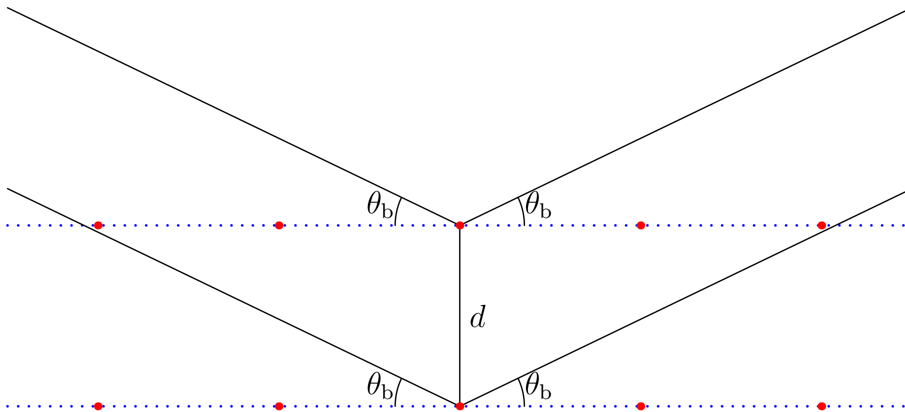

Figure 2.10: Description of Bragg's law. d is the distance from an atom plane to another. θ is the angle of the incident and scattered beam. λ is the wavelength of the plane wave.

consisting of less than a few thousand atoms. Thus for characterizing structures smaller than 200 nm one needs to use something other than visible light. There are many possibilities: e.g. neutrons, high energy photons or electrons. All these can be used to examine structures on the nanometer-scale and all have pros and cons, however electrons have some very attractive properties which make them well-suited for the problem at hand: the ease of handling electrons make imaging an easy task.

The relativistic equation for calculating an electron's de Broglie wavelength can be seen in eq. (2.5), where h is the Planck constant, m_e is the mass of the electron, K is the kinetic energy of the electron and c is the speed of light.

$$\lambda = \frac{h}{2m_eK\left(1 + \frac{K}{2m_ec^2}\right)}. \tag{2.5}$$

For an electron accelerated by a 200 kV potential, which is a fairly common acceleration voltage, the wavelength becomes 0.002 51 nm. This is much smaller than an atom, thus it is, at least theoretically, possible to resolve individual atoms using a TEM. As we'll see there are other factors which severely limit the resolution, such as the lenses.

2.4.3 Electron optics

A VLM uses glass lenses or mirrors to focus the beam, while a TEM uses electromagnet lenses to achieve this. The quality of the electromagnetic lenses are much poorer compared to the lenses used in VLMs[2]. The poor quality of the lenses greatly limit the possible resolution in a TEM, making it very hard to achieve atomic resolution. Fairly recent developments have enabled the production of lenses

[2]Sometimes compared to using the bottom of a soda-can as a lens.

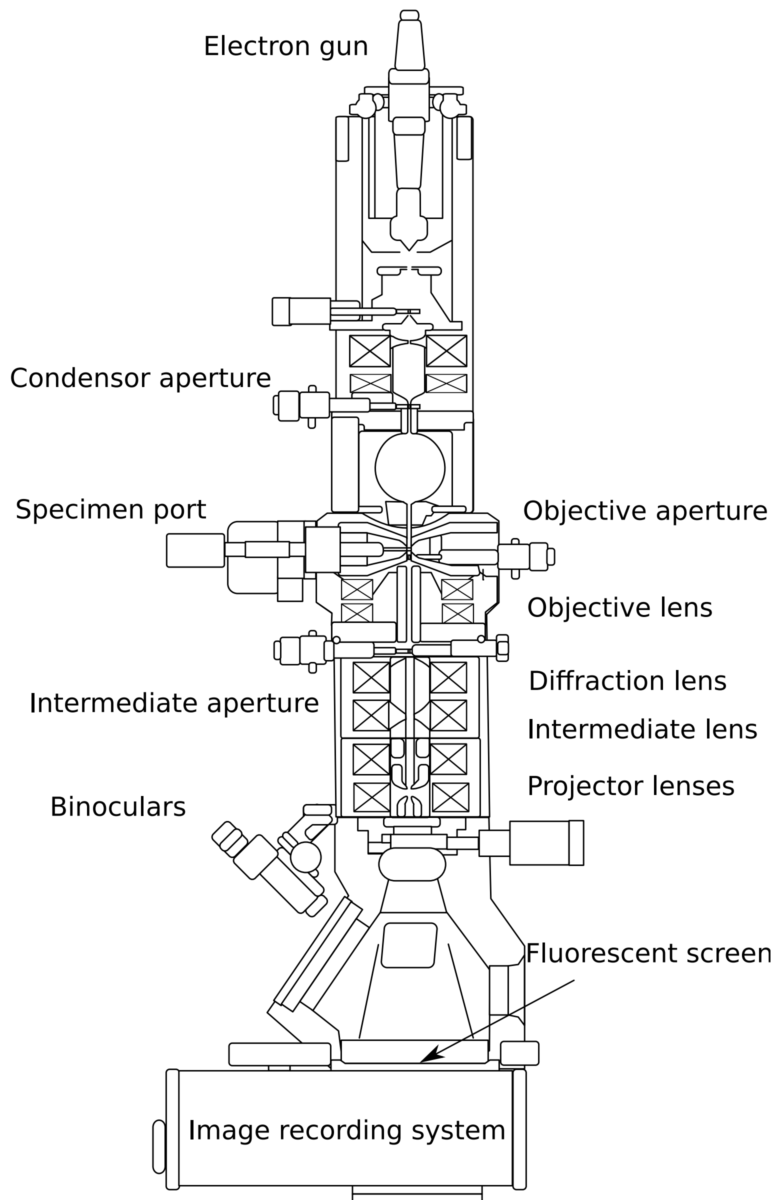

Figure 2.11: Schematic of the optical components of a basic TEM. Figure from Wiki Commons[7]

which correct for different aberrations. Reducing these aberrations have enabled the imaging of even smaller features, down to ångstrom sizes[35]. The electron microscopes used in this thesis were equipped with such aberration correctors, and will be discussed section 2.4.7.

A layout of the optical components of a basic TEM can be seen in fig. 2.11. Even though TEMs and VLMs work by different mechanisms (electrons vs. photons), it is possible to use the same formalism developed for VLMs to explain how the electrons will behave in a TEM. A simple ray diagram is shown in fig. 2.12. The image plane is where the magnified image of the object will be formed. The back focal plane is where the parallel beams from the object plane will intersect, which leads to the diffraction pattern being formed here.

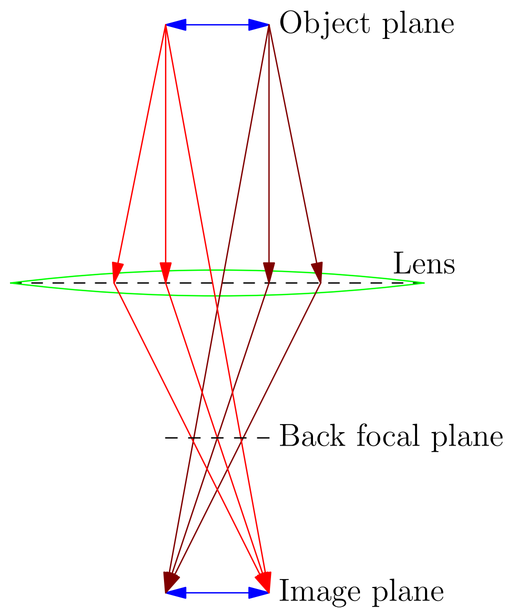

Figure 2.12: Showing how rays from two points of the object define the important optical planes: object, back focal, lens and image plane.

By changing the strength of the lenses it is possible to image the diffraction pattern, which can be used to orient the material in the right direction. For example a zone axis, which is shown in fig. 2.13.

2.4.4 Image contrast

Contrast is the difference in intensity between two areas in proximity to each other, the higher the contrast the easier it is to distinguish them from each other. This is central in all forms of imaging, and knowing the different effects which create them is an essential skill.

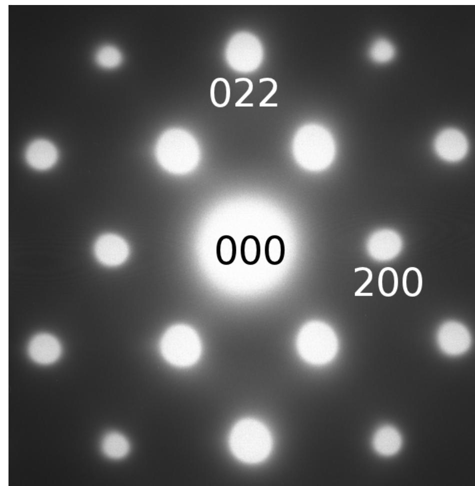

Figure 2.13: Diffraction image of GaAs. Image taken with the electron beam parallel to the [110] zone axis. The numbers show some Bragg reflections.

Many different processes scatter electrons, and all of these contribute to contrast in a TEM. One of them is the mass-thickness contrast which is caused by incoherent inelastic scattering, and is highly dependent on the atomic number[3] and the thickness of the sample. Thus elements with higher atomic number will scatter more compared to elements with lower atomic number. The more material the electron has to travel through, the more likely it is to be scattered.

Another source of contrast is diffraction. When the electron beam is parallel to a zone axis scattering due to diffraction will occur. This effect is strongest in crystalline samples and will scatter electrons as described by Bragg's law.

There are several other processes which produce contrast, but the ones covered here should suffice for this thesis.

2.4.5 High-Resolution Transmission Electron Microscopy

High-resolution Transmission Electron Microscopy (HRTEM) is an imaging technique which uses phase changes to yield information. This type of imaging is often called phase-contrast imaging. This imaging technique was not used extensively in this thesis, and can be read about in Williams and Carter[33].

Phase-contrast makes HRTEM images notoriously hard to interpret, necessitating the use of simulations (section 2.6).

[3] Often called Z-contrast

2.4.6 Scanning Transmission Electron Microscopy

STEM is an imaging mode avaliable in many TEMs. Usually the sample is aligned to a zone axis by using diffraction in regular TEM mode, and then the device is switched to STEM mode. This kind of device is called a TEM-STEM, which uses high energy electrons. Another type is a SEM-STEM, which uses low energy electrons. A TEM-STEM was used in this thesis, so from now on STEM will refer to a TEM-STEM.

The basic difference between Scanning and "regular" TEM mode is how the electron beam is used: in STEM the electron beam is focused to a narrow spot, which is scanned in a raster pattern over the area being imaged. The inner workings of a STEM and an example of a raster scan pattern is shown in fig. 2.14. The beam

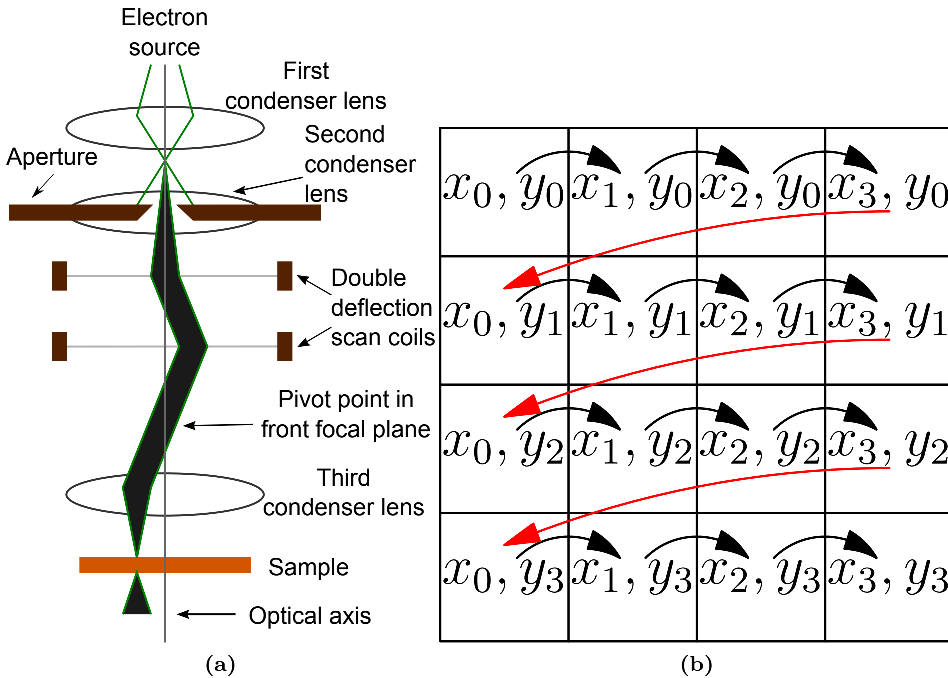

Figure 2.14: (a) Schematic of the inner workings of a STEM. The scan coils scan the beam in a raster pattern shown in (b). Having two scan coils ensure the beam is kept parallel to the optical axis. Figure courtesy Martin Ervik. (b) Showing a raster scan pattern in the sample plane. The beam starts at (x_0, y_0), then goes to (x_1, y_0). This continues until it reaches x_{max}, then it jumps back and down to (x_0, y_1), shown with a red arrow. These two processes repeat themselves until the probe reaches (x_{max}, y_{max}) which is (x_3, y_3) in this example.

must be kept parallel to the optical axis to ensure the beam intercepts the sample at the same angle. After the beam has interacted with the sample, the electron signal is collected in several different detectors. This will be discussed later. This method avoids the need for a lense to form the image, which is required in TEM

mode. Thus removing one source of aberrations, reducing the amount of noise in a STEM image. One large advantage of STEM is its relative straight forward interpretation: HRTEM images are based on phase-contrast which can vary greatly and be caused by *many* different effects; STEM images are based on the electron count from one small part of the sample. This cause the final image to be less dependant on sample thickness and TEM focus setting.

One issue with STEM is imaging instability. Imaging instability refers to unintended movement of the sample while inside the STEM. One source of instabilty is thermal expansion. The cause of thermal expansion is a temperature gradient in the sample holder. Thermal expansion is usually a small effect, however, at very large magnifcation this becomes a serious issue. The issue is solved by letting the temperature in the sample holder reach equilibrium. Another source of instability is vibrations. This can be caused by many different objects e.g. motor vehicles, machinery, trains. An easy, albeit costly, solution is placing the STEM in a vibration damped structure. The issue of imaging stability is not unique to the STEM. It also occurs in HRTEM and regular TEM, but imaging in STEM ususally takes longer time. The longer the imaging time, the larger these instability issues become. There are primarily two types of detectors which can be used in

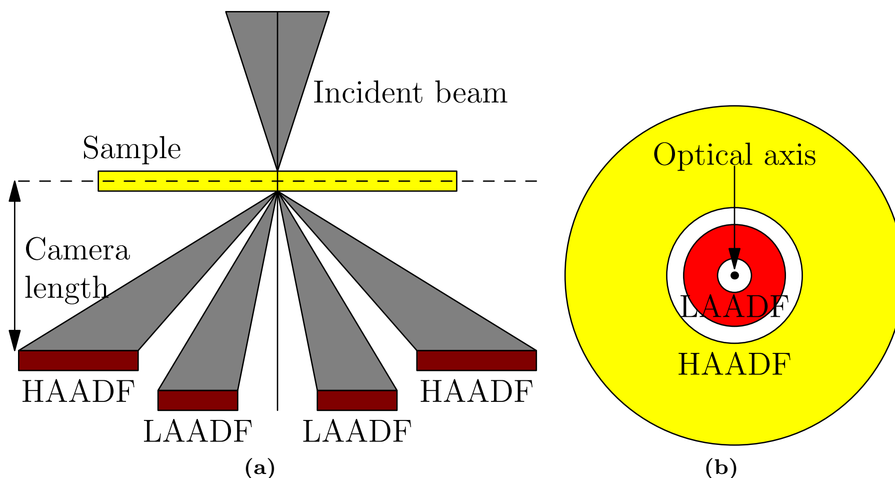

Figure 2.15: (a) Schematic of incident electron beam hitting the sample and electrons scattering into the LAADF or HAADF detectors, shown from the side. Also shown is the the camera length, which is the distance from the sample to the detector. (b) Schematic of the detectors in (a), from a topside viewpoint. The HAADF detector is much larger than the LAADF detector.

a STEM: bright field and annular dark field (ADF). ADF is commonly divided into two subcategories: high-angle annular dark field and low-angle annular dark-field . LAADF is often simple referred to as ADF, however in this thesis ADF will refer to the supergroup consisting of LAADF and HAADF. Only ADF detectors were used in this thesis, so the discussion will focus on this detector type. For a brief overview of the different detectortypes, see Willians and Carter[33, p. 159].

Annular Dark-Field

The ADF is a common detector to use in a STEM, and is shaped like an annulus with the optical axis as the center. This arrangement is shown in fig. 2.15b. This geometrical form causes the detector to collect all electrons which are scattered between the detector's inner and outer radius, as shown in fig. 2.15a. The scattering angle of these electrons is the important parameter, and is easily calculated from the inner and outer radius and the camera length. This calculation gives two values: the inner and outer detector angle. These two angles are extremely important since different electron scattering events have different angular distributions. This angular distribution enables collection of electrons scattered by specific processes, and is easily accomplished by changing the camera length. The camera length is varied by raising or lowering the detector.

Image contrast in STEM

There are several interactions which lead to contrast in STEM: diffraction, strain and Z-contrast. The diffraction contrast was discussed in section 2.4.1 and is a low-angle scattering event, below 50 mrad[33, p. 379]. Strain contrast is also a low-angle effect. The Z-contrast arise mostly from thermal diffuse scattering, and is highly dependent on the atomic number and the thickness of the sample. Elements with higher atomic number will scatter more, compared to elements with lower atomic number. The Z-contrast is usually the dominant scattering event at angles higher than 50 mrad. By collecting the high-angle scattered electrons, it is possible to infer the atomic number from a STEM image.

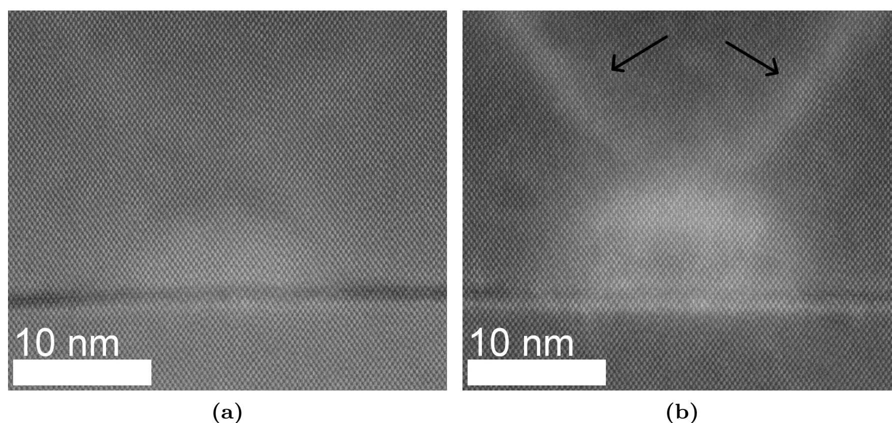

(a) **(b)**

Figure 2.16: (a) HAADF-STEM image of two stacking faults originating in a QD, and a wetting layer. (b) LAADF-STEM image of the same area as in (a). The arrows mark the location of the stacking faults.

Figure 2.16 shows HAADF and LAADF images of the same area. The biggest difference is the visibility of the stacking faults. In fig. 2.16a they are barely visible,

while they're clearly visible in fig. 2.16b. Another difference is the contrast at the wetting layer which is better in fig. 2.16a.

Even though electrons scattered due to strain are too low-angle to impact a HAADF detector, they will still effect contrast when using a HAADF. One of these effects is the reduction of channeling. Channeling can be described in a simple fashion: an electron beam aligned parallel to an atom column be "channeled" along the atom column. If the electron beam is channeled close to the atom column, the amount of electrons scattered at high angles will increase. However if parts of the atom column is strained, this channeling effect will be reduced[36]. Therefore strain will alter the intensity in HAADF images. Channeling is a complicated subject, and will not be discussed in any further detail. For some more information about channeling see[36].

High-Angle ADF

The HAADF detector is a subset of the ADF detector, which collects electrons which are scattered more than 50 mrad. The detector is usually covering a large angle: from 50 to 300 mrad. The electrons scattered due to diffraction or strain have too low angle to hit the detector. The only major effect left is the Z-contrast, which allows the HAADF detector to give information about the chemical composition of a sample.

2.4.7 Aberration correction

One limiting factor in imaging very small features are aberrations. There are two primary aberrations in TEM: spherical and chromatic. Chromatic aberrations occur when electrons with different energies pass through a lens: the electrons will be bent differently depending on their energy. Spherical aberrations are caused by electrons which are not on the optical axis, called off-axis electrons. Off-axis electrons are bent more strongly than electrons closer to the optical axis. Spherical aberrations are usually the dominant aberration, and were corrected for in the TEMs used in this thesis. A spherical aberration corrector works by creating a concave lens which re-converges the off-axis electron beams. This is achieved by using quadru-, hexa- and/or octopole electronmagnet lenses. This is done differently in HRTEM and STEM:

The largest distortion in a HRTEM originates in the objective lens: the lenses following the objective lens will magnify these distortions. The corrector for a HRTEM must therefore be placed after the sample, to correct for these distortions. Such correctors are often called image C_S correctors. A STEM does not require the same aberration correction as a HRTEM, since it does not require imaging lenses. The issue in a STEM is having as small a probe as possible, while still having enough electrons to get a strong signal. This is achieved by placing a corrector between the second condensor lens and the deflection scan coils. This is often called probe C_S corrector.

The inner workings of these aberration correctors are highly complicated, and are outside the scope of this thesis. Simply put: having properly calibrated correc-

tors allows imaging of sub-ångstrom features in both STEM and HRTEM. For a thorough introduction to aberration-correction in TEMs see *Aberration-Corrected Imaging in Transmission Electron Microscopy* by Rolf Erni[37].

2.4.8 Electron Energy Loss Spectroscopy

Electron Energy Loss Spectroscopy (EELS) is a method which utilizes the inelastically forward scattered electrons in a TEM. This signal can serve many different analytical purposes: obtaining chemical composition, information about the electron bonds or determining the thickness of the sample. Only thickness determination was used in this thesis, so the discussion will focus on that topic. Calculating the thickness t is done by using

$$t = \lambda_p \ln \left(\frac{I_T}{I_0} \right) \tag{2.6}$$

where λ_p is the mean free path of the plasmons, I_t is the total integrated intensity and I_0 is the intensity of the zero-loss peak[38, p. 361]. The intensities I_t and I_0 are retrieved from an EELS spectrum, while the λ_p is a bit more tricky. The ideal way of getting a value for λ_p would be from experimental calculations. However the value was not found for our specific experimental parameters, thus a different approach was used where λ_p is calculated from the constituent atoms[39, p. 305]:

$$\lambda_p = \frac{106 F E_0}{E_m \ln \left(\frac{2\beta E_0}{E_m} \right)} \tag{2.7}$$

$$F = \frac{1 + \frac{E_0}{1022}}{1 + \left(\frac{E_0}{511} \right)^2} \tag{2.8}$$

$$E_m = 7.6 \left(\frac{\sum_i f_i Z_i^{1.3}}{\sum_i f_i Z_i^{0.3}} \right)^{0.36} \tag{2.9}$$

where F is a relativistic factor, E_0 is the energy of an unscattered electron in keV, β is the semiangle of collection in mrad, E_m is the average energy loss in the sample, f_i is the atomic fraction of the element i and lastly Z_i the atomic number of element i. Combining Equations (2.7) to (2.9) yields an equation for finding λ_p if the material composition, collection semiangle and unscattered electron energy is known. The two last ones are instrumental parameters which are always known, in contrast with the first one which depends on the sample. Luckily the material composition in certain parts of the sample was known to a high certainty.

2.5 Geometrical phase analysis

Geometrical phase analysis is a method for quantitativly measuring the displacement and strain field in HRTEM and STEM images.

In an image where the atom columns are visible it is possible to get information about the spatial frequencies in the image. This is achieved by Fourier transforming the image to the frequency domain, which results in something similar to a diffraction image as shown in fig. 2.17.

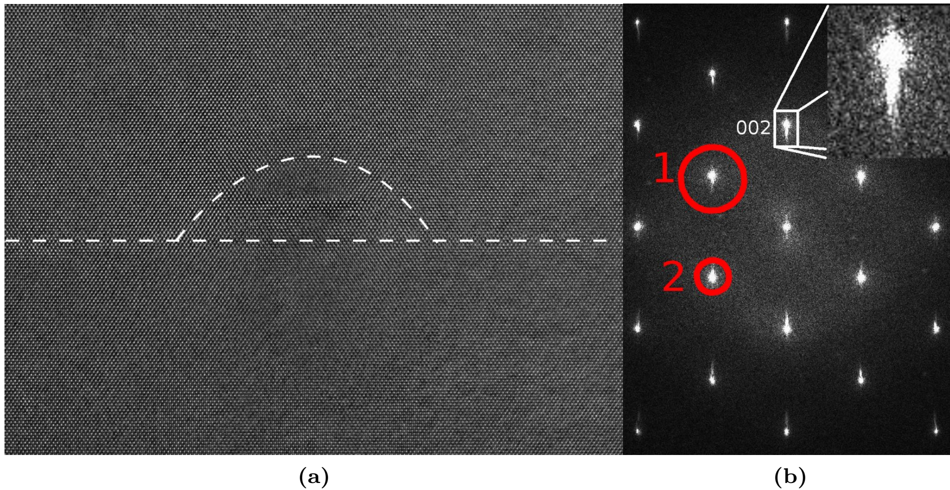

Figure 2.17: (a) A HRTEM image of a quantum dot. Outline showing the wetting layer and the quantum dot. (b) Fourier-transform of (a). Inset: larger version of the {002} Bragg reflection. (1) A large mask. (2) A small mask.

The Bragg reflections infer the mean lattice distances in the HRTEM image. Analysing the signal around the Bragg peak in the inset in fig. 2.17b can yield information about the local lattice structure by using the following method.

1. Filter (mask) away everything expect one Bragg reflection, and its surrounding area.
2. Inverse Fourier transform the filtered image.
3. Map the phase of the inverse Fourier transform.
4. Choose an area to serve as a reference.

The result of this process is seen in fig. 2.18a: a filter has been used to exclude everything in fig. 2.17b except the {002} Bragg reflection; the image has been inverse Fourier transformed and the phase has been mapped. The size of the mask in step 1 is an important parameter: having a large mask will give larger spatial resolution, but may also include more noise. Having a smaller mask will give lower spatial resolution, but may include less noise. An example of large and small mask is shown in fig. 2.17b.

By using phase images it is possible to generate a *strain image*. This is achieved by making another phase image from a non-colinear Bragg peak in fig. 2.17b. With

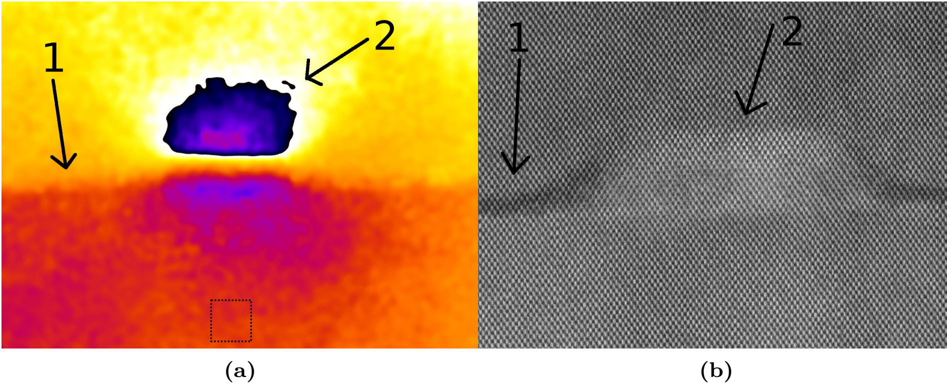

(a) (b)

Figure 2.18: (a) Phase map of the inverse Fourier tranform of fig. 2.17b, using the {002} reflection. (1) Showing the phase shift from red to yellow. (2) Showing a large phase shift, causing a discontinuity in the phase value. The black outline shows the reference lattice. (b) HAADF image of the same quantum dot (1) as in fig. 2.17a for comparison. (2) shows the wetting layer.

these two phase images it is possible to calculate the 2-dimensional strain tensor, which is shown in fig. 2.18. This strain tensor can be interpreted as the percent amount the local lattice deviaties from a reference lattice. It is possible to infer correlations between the features in figs. 2.18a and 4.6c: the phase at (1) correspond to the wetting layer; (2) correspond to the QD.

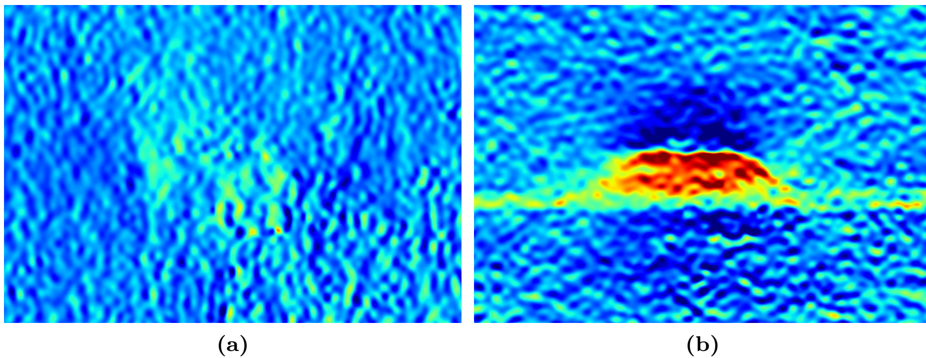

(a) (b)

Figure 2.19: 2-dimensional strain tensor using {111} and $\{11\bar{1}\}$. x-direction is defined as horizontal, y-direction vertical. (a) ε_{xx}. (b) ε_{yy}.

Even though HRTEM images have been used for as an example it is possible to use high-resolution STEM images as well. In fact STEM images are far superior under certain conditions, as shown in chapter 3.4

2.6 Multislice simulations

2.6.1 Some background on simulations

There are *many* effects which contribute to the contrast in TEM and STEM images. Interpreting these images can be very complicated. One way to solve this issue is by simulating how the electron microscope will image the sample.

There are generally two different ways of performing such simulations: solving the Schrödinger equation for the system analytically or numerically. The analytical way can yield insight into the scattering processes, but if the system becomes too large the equation may become impossible to solve. The system examined in this thesis was considered too large for analytical methods, so a numerical technique was used: the multislice method.

2.6.2 The multislice method

As noted in section 2.4.1, electrons interact heavily with most materials. This can cause electrons to be scattered multiple times if the sample is sufficiently thick. Let's first look at a sample which is sufficiently thin i.e. where the weak phase object approximation is valid. For derivation and more information about the weak phase object approximation see Williams and Carter[33, p. 486] or Kirkland[40, p. 78]. In this approximation the majority of the electrons pass straight through the sample. This makes the probability of an electron experiencing several scattering events negligible. Under such conditions the first order Born approximation is valid[41, p. 616],

$$f^{\mathrm{B}} = \frac{1}{4\pi} \int \exp\left(i\left(\mathbf{k_1} - \mathbf{k_2}\right) \cdot \mathbf{r}\right) U\left(\mathbf{r}\right) \mathrm{d}^3\mathrm{r}. \tag{2.10}$$

where $\mathbf{k_1}$ is the wave vector for the incoming electron and $\mathbf{k_2}$ is the wave vector for the scattered electron. $U(\mathbf{r})$ is the potential at position $\mathbf{r}$. f^{B} is the scattering amplitude, where the superscript B refers to the first order Born approximation. The scattering amplitude basically describes how many electrons are scattered in each certain direction. By inserting values for electron scattering and reordering some a little bit,

$$f^{\mathrm{B}} = \frac{1}{2\pi e a_0} \int \exp\left(i 2\pi \mathbf{q} \cdot \mathbf{r}\right) U\left(\mathbf{r}\right) \mathrm{d}^3\mathrm{r}. \tag{2.11}$$

Which is the 3D Fourier transform of the atomic potential [40, p. 86]. This is very advantageous because there exists highly optimized numerical methods for calculating the Fourier transform. In addition Fourier transforms are very easy to implement in a parallel fashion, meaning one can utilize several CPUs or GPUs for decreased computation time.

Unfortunately eq. (2.11) does not correctly calculate the phase of the scattering amplitude. A different (but similar) formula is used for the scattering events, where the Fourier transform can still be utilized. This enables a high degree of parallelization.

The formalism above works for thin samples, where the electrons experience maximally one scattering event. However multiple scattering events per electron is common, thus this formalism is not good enough. The issue is solved by splitting the thick sample into multiple thin slices, hence the term multislice. By making each of the slices sufficiently thin, one can make the weak phase object approximation valid for the slices. This makes it possible to utilize the method explained in the previous paragraph. The slicing of the sample is shown in fig. 2.20.

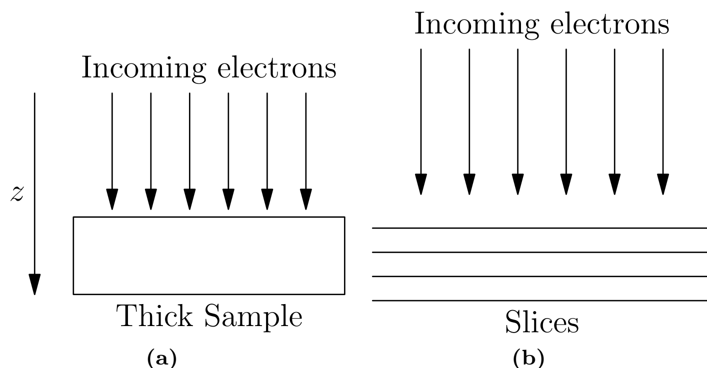

Figure 2.20: (a) A 3-dimensional atomic potential representing a thick sample. (b) The thick sample split into several “slices”. z-axis parallel to the incoming electrons.

The process for regular TEM can be summarized as follows:

1. Dividing the full atomic potential into smaller parts in the z-direction. The smaller parts are then each projected onto a 2-dimensional plane making them “slices”.

2. The incoming electrons are modelled by a plane wave, which is transmitted and propagated through the first slice. This is done by using the Fourier transform formalism explained earlier.

3. Take the the exit wave from the first slice, and propagate it through the second slice. This is repeated for the remaining slices.

4. Apply the transfer function for the objective lens.

5. Some post-processing yields the image.

The multislice process for STEM is similar to that of the TEM one:

1. Dividing the full atomic potential into smaller parts in the z-direction. Then the smaller parts are each projected onto a 2-dimensional plane making them “slices”.

2. Calculate the probe wave function at the first scan position (see section 2.4.6).

3. Transmit and propagate the wave function through all the slices.
4. Integrate the intensity incident on the detector. This becomes *one* pixel on the final image.
5. Some post-processing yields the image.

One large difference between the TEM and STEM simulations is the amount of simulations needed: in STEM *every* pixel requires its own simulation. This will be discussed further in section 3.5.4.

2.6.3 Frozen-phonon method

An important parameter is the thermal motion of the atoms. This motion cause the atoms to become "blurred" in the images, creating a less clearly defined image of the atom columns. The thermal motion not only varies between the different atoms, but the neighboring atoms as well: the As atoms in GaAs will have different thermal motion compared to As in InAs. This is taken into account by using a method called the frozen-phonon method:

An atomic structure is generated where the atoms are displaced randomly, according to a root-mean-square displacement distribution. This atomic structure is called a phonon-configuration. Then a multislice simulation is performed on the atomic structure. Generating several such phonon-configurations and running simulations on them yield the final image: an image which is the average of all the phonon-configurations.

Chapter 3

Method and experiment

3.1 Samples

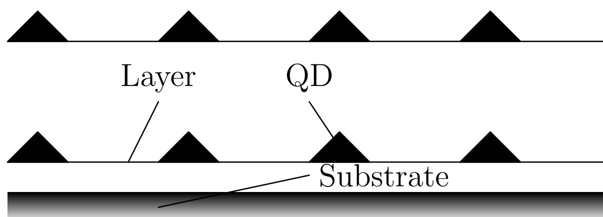

Figure 3.1: Schematic of the growth of a QD sample using Stranski-Krastanow (S-K) growth mode. Spacer material grown in between the layers containing QDs. In this project the QDs consisted of InAs. One of the samples had GaAs as spacer material, the other sample had AlGaAs as spacer material.

Two different samples were examined in this thesis. The primary difference between these two samples was the "capping". Capping refers to the material grown directly after an InAs layer. This is seen in tables 3.1 and 3.2 where the former has a 3 monolayer thick layer of AlAs. This sample will be referred to as the AlAs-capped sample, while the other sample will be referred to as the GaAs-capped sample.

Both samples examined in this project were made at NTNU by Sedsel Fretheim Thomassen with an MBE.

Figure 3.1 show the following process: spacer material grown on the substrate, with S-K "islands" grown afterwards, then spacer material and lastly another "island" layer.

The motivation for having a layer of AlAs after the InAs is the aluminum's shorter diffusion length compared to In and Ga. This should cause indium to diffuse less[42], retaining a greater amount of indium inside the quantom dots.

Table 3.1: Growth parameters for the AlAs-capped sample. Grown on a n-doped GaAs(100) substrate.

Material	Thickness	Growth temp., °C	Growth rate, ML/s
GaAs (buffer)	100 nm	about 590	1
InAs	2.8 ML	500	0.1, cyclic
AlAs	3 ML	500	1
GaAs	10 nm	500	1
GaAs	70 nm	590	1
InAs	2.8 ML	500	0.1, cyclic
AlAs	3 ML	500	1
GaAs	10 nm	500	1
GaAs	40 nm	590	1
InAs	2.8 ML	500	0.1, cyclic

Table 3.2: Growth parameters for the GaAs-capped sample. Grown on a n-doped GaAs(100) substrate.

Material	Thickness	Growth temp., °C	Growth rate, ML/s
GaAs (buffer)	100 nm	about 590	1
InAs	2.3 ML	512	0.1, cyclic
GaAs	10 nm	512	1
GaAs	40 nm	590	1
InAs	2.3 ML	512	0.1, cyclic

Figure 3.2a shows a unit cell of the zinkblende structure tilted so that the $[0\bar{1}1]$ zone axis points into the paper. Figure 3.2b shows a HAADF-STEM image tilted in the same way, where the electron beam was parallel to the $[0\bar{1}0]$ zone axis. "Dumbbells" are highlighted with red boxes in both figures. Dumbbells appear when a zinkblende structure is tilted in certain directions and projected onto a plane, e.g. a TEM image. The dumbbells in the inline in fig. 3.2b consists of a Ga and an As atom, but the Ga can be substituted by either Al and In in this sample. Important zone axes shown in figs. 3.2a and 3.2b include the [100] and the [110] zone axis. The [100] zone axis is parallel to the growth direction, which is parallel to the ε_{yy} strain direction and is parallel to the vertical axis on all TEM images in this thesis. The [011] zone axis is parallel to the growth plane, which is parallel to the wetting layer and parallel to the horizontal axis on all the TEM images in this thesis. All TEM images in this thesis were taken with the electron beam parallel to the $[0\bar{1}1]$ zone axis.

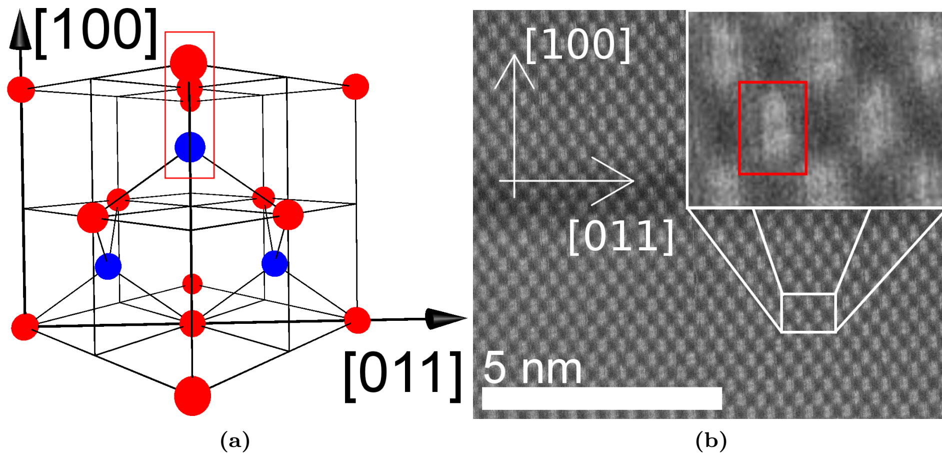

(a) (b)

Figure 3.2: (a) Illustration of the zinkblende unit cell tilted so that the $[0\bar{1}1]$ zone axis goes into the paper. The red box shows a "dumbbell". (b) HAADF-STEM image tilted similarly as (a). The [100] zone axis, which is parallel to the growth direction, is shown on the image. The electron beam was orthogonal to both the [100] and [011] zone axes, making it parallel to the $[0\bar{1}1]$ zone axis. The inline figure shows a magnified part of the HAADF image, with the red box showing a dumbbell.

3.2 Sample preparation

TEM samples have to be electron transparent. To achieve electron transparency the thickness the samples must be below about 100 nm in the areas one wants to examine. The process of making samples varies greatly in complexity and time depending on the material's properties.

The samples of interest in this project were grown as thin films on a substrate

and the goal was to analyze the cross section of the thin film. There are basically two steps: making the sample fit inside a 3 mm diameter sample holder, then making the sample sufficiently thin. To achieve this the so-called sandwich method was used, where the process is as follows:

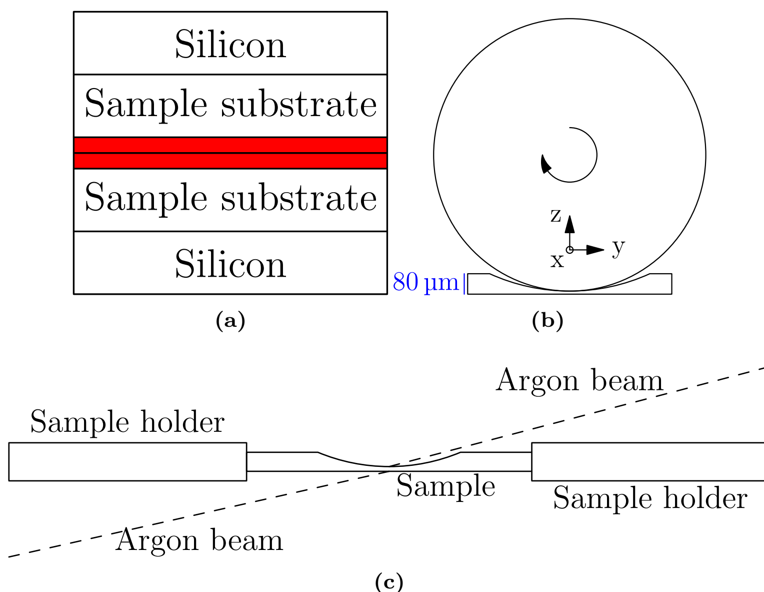

Figure 3.3: Illustrations of different steps in the sample preparation process. Note that the figures are not to scale. (a) Schematic of the sandwich method. With the thin films (red) facing each other. (b) Shows the dimpling process, with the sample being rotated about the z-axis. The dimpler disk is represented by the circle. (c) Shows the ion milling process, where argon atoms are shot at an angle of 4° towards the middle of the specimen.

1. The sample was received as a piece of a wafer. First a piece of is heated to about 140 °C, then wax is applied to it. The wax will then melt, and the wafer is placed on the melted wax. Next the glass piece is cooled, which causes the wax to solidify thus fastening the wafer.

2. With the glass piece as support, two rectangular pieces with dimensions 3 mm times approximately 1 cm are cut from the wafer, using a 150 µm Allied High Tech diamond saw. In addition two similar pieces are cut from a silicon wafer. Next the pieces are glued together with EpoxyBond 110 from Allied High Tech in the following order (see fig. 3.3a): silicon piece, sample piece with thin film upwards, sample piece with thin film downwards, silicon piece. The glue layer was very thin, due to the pressure applied to the "sandwich". The glue is hardened by heating it.

3. The "sandwich" is polished to make it fit into a brass cylinder with an outer diameter of 3 mm. When the "sandwich" has the correct dimensions the

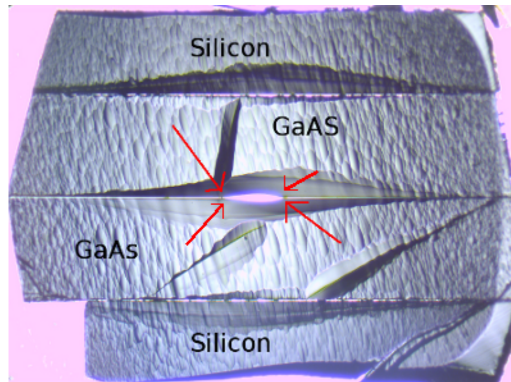

Figure 3.4: A TEM specimen, after all sample preparation steps. Arrows marking the possible areas for TEM imaging of the quantum dots.

cylinder tube is filled with the same type of glue as used earlier, and the "sandwich" is placed inside the cylinder. Then the glue is hardened by heating it.

4. The cylinder is cut into slices of about 0.8 mm along its rotational axis with the same diamond saw as used earlier.

5. Through visual inspection the slice with the least amount of defects is selected, which will be referred to as the specimen.

6. The specimen is then polished down to a thickness of about 80 µm by using grinding paper, starting with paper with a grain density 2500 cm^{-2} and finishing with grinding paper with grain density 4000 cm^{-2}. During the polishing process water is continuously applied to the grinding paper to achieve a smooth surface on the specimen. The height of the specimen is checked with a VLM.

7. A dimple is made in the specimen by using an EAF Instruments Model 2000 dimpler, see fig. 3.3b, where 1 µm Allied High Tech diamond paste is used. The thinnest piece of the specimen was about 30 µm.

8. The last step is ion milling using a Precision Ion Polishing System Model 691 from Gatan, cooled with liquid nitrogen. The goal is to make a small piece of the thin film electron transparent, this is achieved by milling a small hole in the border between the thin films. Argon atoms are accelerated by voltage of 3.5 keV shot at the specimen, see fig. 3.3c. The specimen is ion milled until it is possible to see an extended hole in the sample, as shown in fig. 3.4.

The end result should be a specimen with four possible locations for analysis with a TEM. These areas are shown in fig. 3.4, marked by the arrows.

One effect of thinning the sample might be the relaxation of structures created by strain, causing the strain imaged in the TEM to not necessarily be the same as the strain in the sample before the preparation. This process is often refered to as surface relaxation.

3.3 Experimental equipment

Three different electron microscopes were used in this thesis: a Jeol 2010F, a FEI Titan 80-300 with probe C_S corrector, and a FEI Titan 80-300 with image C_S corrector. The Jeol was used for checking the quality of the samples, and provided overview images (fig. 4.1). It was operated at a acceleration voltage of 200 kV.

The two Titans were located in the Center for Electron Nanoscopy (CEN) at Technical University of Denmark (DTU) and were operated by Chris Boothroyd. The Titan with probe-correction was used to obtain STEM images. The Titan with image-correction was used to obtain HRTEM images and EELS spectra. Both microscopes were operated at a acceleration voltage of 300 kV. Both microscopes had a field emission gun (FEG). For full specifications on the Titan microscopes see the CEN webpages: probe-corrected Titan[43] and image-corrected Titan[44].

3.4 Geometrical Phase Analysis

All GPA were done using the plugin “GPA for Digital Micrograph v3.0” from HREM Research Inc.

GPA on some HRTEM images were found to introduce artifacts, which greatly reduced their informational value. The cause of these artifacts seems to be the thickness of the imaged area[45], since images from the thinnest area contained much fewer artifacts. An example of these artifacts is shown in fig. 3.5a

GPA on STEM images were also found to introduce artifacts. The cause of these artifacts is a “flyback”-error[46], caused by the raster scan pattern shown in fig. 2.14b. The jumps indicated by the red arrows is a relatively large beam displacement. The large beam displacement is not as accurate as the jumps indicated by the black arrows, which means the artifacts will occur in the y-direction in fig. 2.14b. Aligning the x-scan direction such that it lies parallel to the strain-direction of interest, solves this issue. The strain was predicted to be parallel to the growth direction. The scan direction was therefore aligned parallel to the growth direction in all the STEM images. This is unfortunately not an optimal solution.

The spatial resolution of the GPA is a function of the mask size (discussed in section 2.5), and will be given at each GPA image. Figure 3.6 shows GPA of the same image, but with two different masks. Figure 3.6a seems to have a larger degree of details. It also seems to contain a larger degree of noise, which is seen in the bottom-right corner with the red peaks.

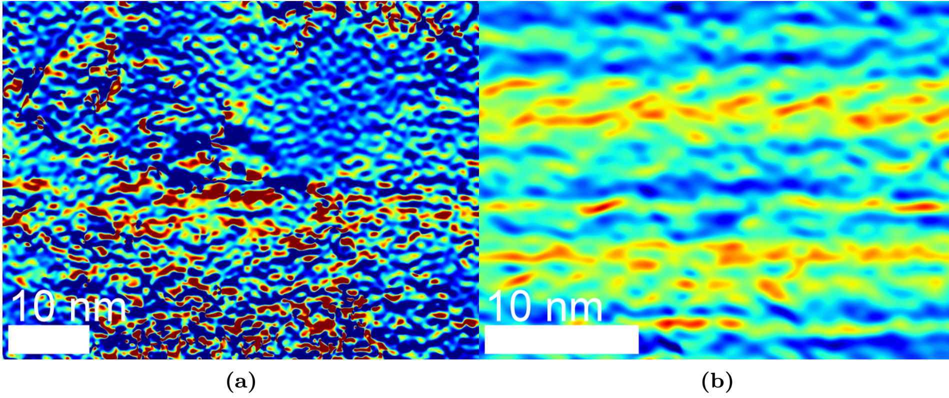

(a) (b)

Figure 3.5: (a) GPA of a HRTEM image, of a thick area. Strain direction ε_{yy}. (b) GPA of a HAADF-STEM image. Same area as (a). Strain direction ε_{xx} which is parallel to the y-direction shown in fig. 2.14b.

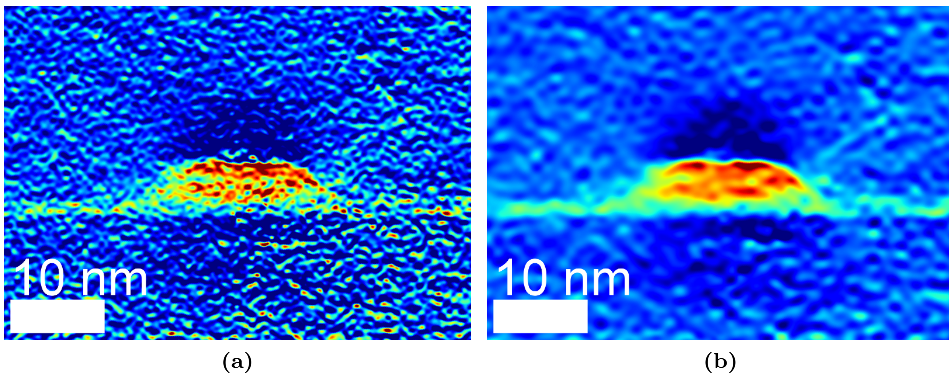

(a) (b)

Figure 3.6: GPA of the same HRTEM image. (a) Large mask. Spatial resolution of 0.658 nm. (b) Small mask. Spatial resolution of 1.32 nm.

3.5 The multislice simulations

All simulations were done using the STEMCuda program made by Christian Dwyer.

Comparing the simulated and experimental data is achieved by normalizing the experimental data. The normalization is performed with regards to the incoming electron beam, using the formula

$$I_{\text{normalized}} = \frac{I_{\text{raw}} - I_{\text{blackcurrent}}}{I_{\text{detector}}} \tag{3.1}$$

$$I_{\text{detector}} = \frac{I_{\text{exp.mean}}}{I_{\text{sim.mean}}} \tag{3.2}$$

I_{raw} is a mean intensity measured in the reference area directly from the STEM data. $I_{\text{blackcurrent}}$ is the intensity measured in an area with complete vacuum. This intensity stems from brightness/contrast settings on the instrument itself. The brightness/contrast settings were not altered during the TEM session, so the $I_{\text{blackcurrent}}$ taken for one image should be valid for all (during the same session). $I_{\text{exp.mean}}$ is the mean intensity of the reference area in the experimental image. $I_{\text{sim.mean}}$ is the mean intensity of a simulated image with identical thickness and composition as the reference area. Combining all these factors in eq. (3.1), yields the normalized intensity $I_{\text{normalized}}$.

The thickness is found by using EELS, and the composition in the reference is assumed to be GaAs. The composition assumption should be valid as long the reference area is far away from the areas with indium or aluminum.

3.5.1 Root-mean-square displacement

The root-mean-square displacement is calculated from the Debye-Waller factor, which is basically a measure of the thermal motion of an atom. Calculating this factor can be very tedious but luckily this has already been done by Schowalter et al[47]. The results of their calculations were a parametrized version of Debye-Waller factor for different semiconductor-materials. The mean-square ($\langle u^2(T) \rangle$) is calculated by using the parametrized data and the formula

$$\langle u^2(T) \rangle = \frac{\hbar}{2M} \frac{\coth\left(\hbar\left(Ae^{-\frac{T^2}{\sigma^2}} + B\right)/2k_{\text{B}}T\right)}{Ae^{-\frac{T^2}{\sigma^2}} + B} \tag{3.3}$$

where A, B and σ are parameters from the paramatrization, M is the atomic mass, T is the temperature, k_{B} is the Boltzmann constant and $\hbar$ is the reduced Planck constant. Using the parameters from Schowalter et al[47] we get the mean-square displacement for a temperature of 300 K in table 3.3.

Figure 3.7 shows two different simulations: one with thermal motion, and one without.

3.5.2 Simulation input parameters

There are two kinds of parameters: instrumental parameters and simulation parameters. The instrumental parameters are given by the settings on the TEM and

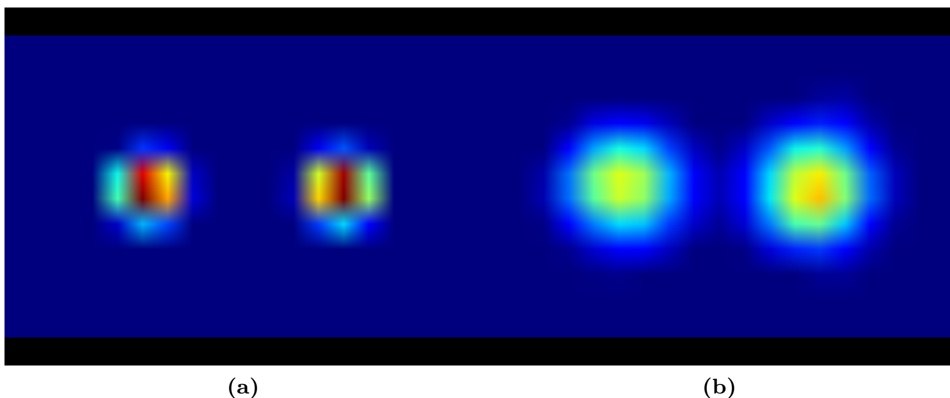

(a) (b)

Figure 3.7: Multislice simulations showing the effect of the debye-waller constant. (a) Debye-waller constant set to 0. (b) Debye-waller constant set to the values for GaAs in table 3.3.

Table 3.3: Calculated mean-square and root-mean-square displacement for GaAs, InAs and AlAs. Calculated by using eq. (3.3) with a temperature 300 K. Parameterization data taken from [47, Table 4].

Element	$\langle u^2 \rangle$ [Å^2]	$\sqrt{\langle u^2 \rangle}$ [Å]
Ga (GaAs)	0.008827	0.09395
As (GaAs)	0.007588	0.08711
In (InAs)	0.012970	0.11388
As (InAs)	0.011065	0.10519
Al (AlAs)	0.008792	0.09377
As (AlAs)	0.007716	0.08784

Table 3.4: The different instrumental parameters used in the multislice simulations.

Name	Acc. voltage	Conv. angle	Defocus	Aber.	Det. ang.
Parameter	300 kV	26.5 mrad	0	0	57 to 363 mrad

Table 3.5: The different simulation parameters used in the multislice simulations. Unit cell size (x,y,z) refers to the size of the GaAs unit cell in the ⟨110⟩ direction. unit cells (x,y) refers to the number of repetitions of the unit cell defined earlier. Pixels is how many pixels the potential is divided into. Slices pr. unit cell defines how thick each slice should be.

Name	Unit cell size (x,y,z) [Å]	Unit cells (x,y)	Pixels (x,y)	Slices pr. unit cell
Parameter	3.995, 5.65, 1.998	5, 5	1024, 1024	2

are usually well-known. The simulation parameters need to be chosen to ensure an optimal result, which can be tricky to choose.

Instrumental

The instrumental parameters include acceleration voltage, convergence angle, aberrations and detector angles. These are shown in table 3.4.

Some comments about the aberration values: the numerical values supplied by the calibration software varied greatly, and was deemed too unreliable to be used in the simulations. This situation was not optimal. The error is minimized by using relative intensities when calculating the chemical composition.

Simulation

The simulation parameters are shown in table 3.5.

3.5.3 Element mixing

Ga, In and Al substitute each other in the zinkblende structure. When doing simulations with a mixed element composition (for example 50% InAs and 50% GaAs), several effects must be taken into account: the Debye-Waller factor in As varies depending on the adjacent elements; the position of the different elements will greatly influence the intensity. The former issue is solved by adding the atoms as pairs. Placing both Ga and As with Debye-waller factor corresponding to GaAs. The latter can be seen in fig. 3.8 where systems with 50% InAs and 50% GaAs have been simulated; (a) has the InAs at the top of the sample; (b) has all the InAs at the bottom of the sample. This issue is solved by randomizing the atomic positions which is called an atomic configuration. The InAs/GaAs/AlAs pairs are kept together during this randomization process. The result of such a randomization process is shown in fig. 3.8c. Then simulations are done for several atomic configurations and

the final image is created by taking the average of them. Both phonon and atomic configurations are varied in each simulation to save computational time.

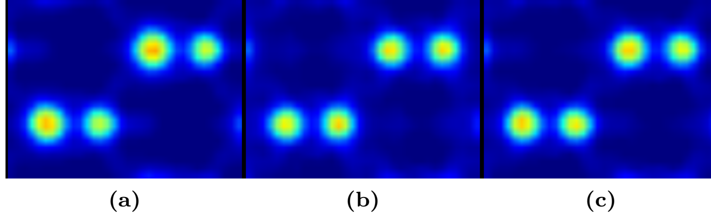

Figure 3.8: Multislice simulations with 50% GaAs and 50% InAs, where the position of the InAs and GaAs has been varied. Simulated with 20 phonon configurations and 30.4 nm thickness. (a) InAs on top, GaAs at the bottom. (b) InAs at the bottom, GaAs on top. (c) Random position for GaAs and InAs.

3.5.4 Probe scanning position

Doing TEM and STEM simulations using the multislice method is fairly similar, but with one important difference: all the pixels in the simulated TEM image are calculated from *one* run through the atomic structure; in the simulated STEM image *every* pixel in the final image requires its own run through the whole atomic structure. Thus STEM simulations are much more time consuming. The run-time scales linearly as a function of the area, thus limiting the simulated area is advantageous. The different elemements were placed randomly, as explained in section 3.5.3, and averaged over multiple atomic configurations. If the averaging is performed over a large amount of atomic configuration, every dumbbell should be essentially identical. Averaging over 32 atomic configurations were found to fulfill the requirement. This meant that simulating over one dumbbell was found to yield the required information, and all simulations were done for one dumbbell. Runtimes for different areas can be seen in fig. 3.9.

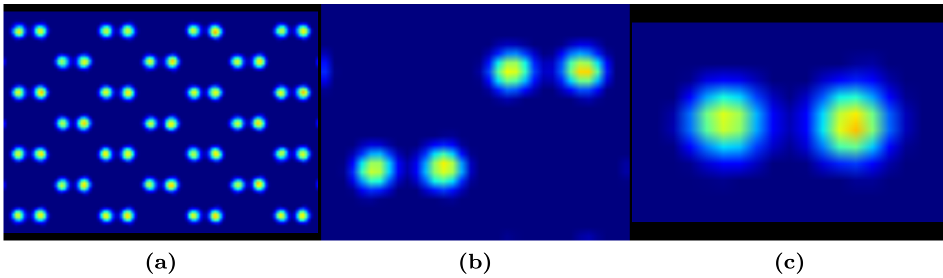

Figure 3.9: Final images of STEM multislice simulations, where different areas have been simulated. 4 phonon configuration. 152 unit cells in the z-direction. 5 unit cells in the x- and y-direction. All images are of GaAs in the $\langle 110 \rangle$ direction. (a) Four dumbbells in the horizontal and four dumbbells in the vertical directions. Runtime: 114 minutes (b) One unit cell. Runtime: 11 min. (c) One dumbbell. Runtime: 2.7 min.

Chapter 4

Results

Two different types of imaging techniques were used: Scanning TEM (STEM) and High-Resolution TEM (HRTEM), which were discussed in sections 2.4.5 and 2.4.6. Figure 4.1 show overviews of the two samples. Figures 4.1a and 4.1c shows the AlAs-capped sample. Figure 4.1b and 4.1c shows the GaAs-capped sample. Quantum dots in fig. 4.1c are numbered for easier referencing. Of special interest are the dislocations in fig. 4.1c. These dislocations originate in QD 5, and seem to end at QD 1 and QD 3.

QD 1: 71 unitcells reference.

4.1 Strain mapping

The strain mapping was performed in two different ways: GPA and analysis of the HRTEM images in reciprocal space. The former is the primary investigative tool, while the latter corroborates the features observed using GPA.

Strain mapping was performed on both the HRTEM and the STEM images, but most of the HRTEM images did not yield any additional information. This was primarily caused by artifacts, as noted in section 3.4. Strain mapping of the HRTEM images were still used for looking at the strain parallel to the wetting layer.

4.1.1 Strain direction

Figure 4.2 shows a representative GPA of a QD in the AlAs-capped sample. The QD is clearly visible in fig. 2.19b, where the strain which is mapped is parallel to the growth direction. Figure 4.2b has negligible amounts of strain. This pattern repeats itself for other QDs in both the GaAs- and AlAs-sample.

4.1.2 Sample comparison

One of the goals of this work is to compare the strain in the two samples. This is divided into two parts. A small section about the wetting layer and a larger section

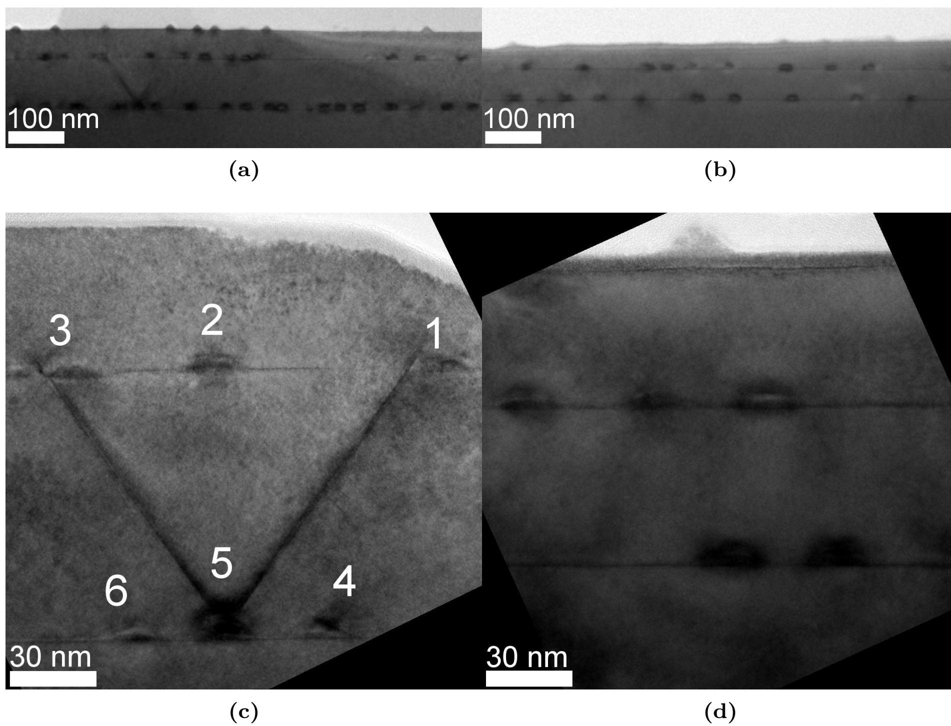

Figure 4.1: Low magnification overview HRTEM images, taken on Jeol 2010F at 200 keV. (a) and (c) shows the AlAs-capped sample at different magnifications. Quantum dots in (c) are numbered for easier reference. Note: (a) and (c) are not from the same area. (b) and (d) show the GaAs-capped sample at different magnifications.

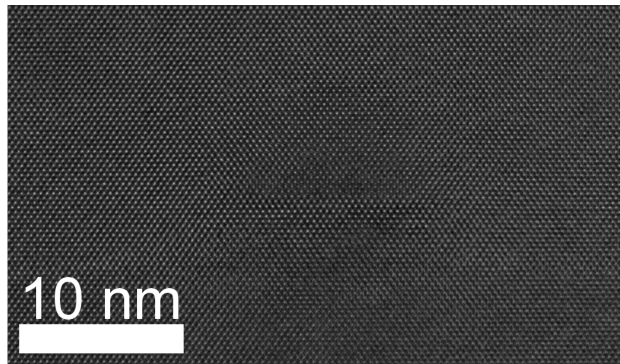

(a)

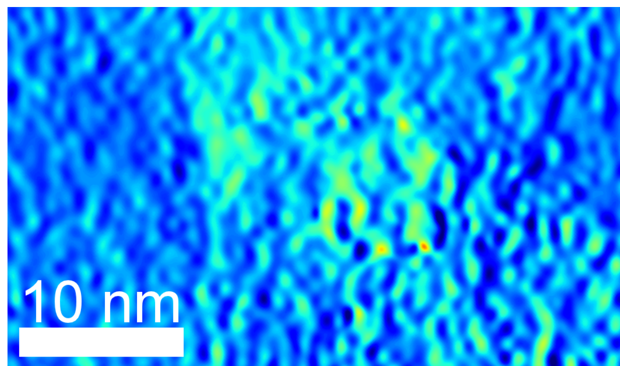

(b)

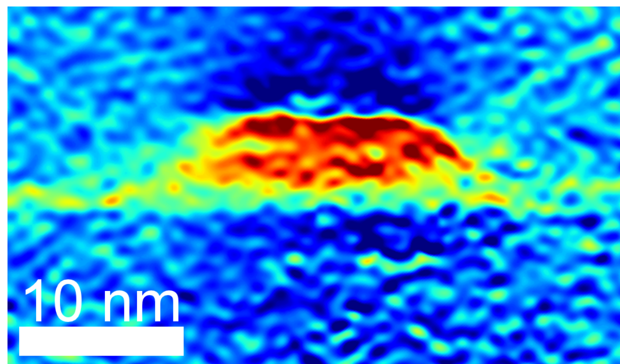

(c)

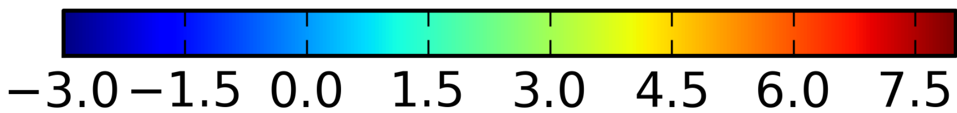

Figure 4.2: (a) HRTEM of QD 2 in the AlGa-capped sample. (b) Shows GPA of (a) in the ε_{xx} direction. (c) Shows GPA of (a) in the ε_{yy} direction. Both GPA with a spatial resolution of 0.988 nm

about the QD themselves.

Strain at the wetting layer

Figure 4.3 shows HAADF-STEM images of the wetting layer on both samples, and strain mapping of the wetting layer. The wetting layer in the AlAs-capped sample seems to have more strain than the GaAs-capped sample. This is confirmed in the line plots in fig. 4.4, which is the vertical average of the strain maps in fig. 4.3.

Two interesting features is marked in fig. 4.4 with arrows. (1) indicates negative strain right before the wetting layer, and (2) indicates a negative strain right after the wetting layer.

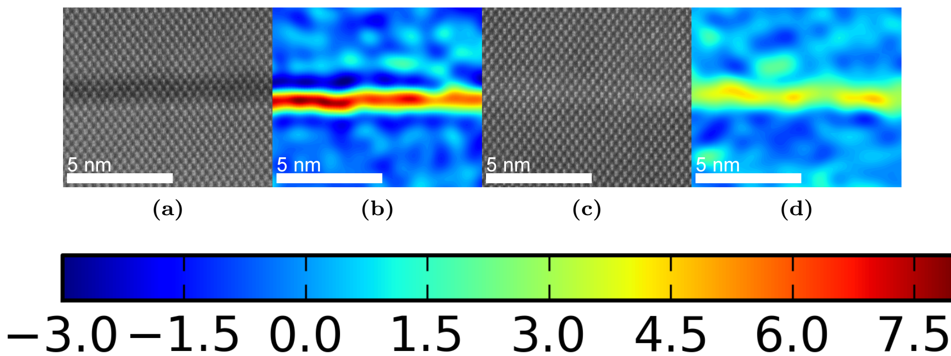

Figure 4.3: HAADF-STEM images of the wetting layer and ε_{yy} strain map of those images. Spatial resolution: 0.978 nm. (a) AlAs-capped sample. (b) GPA of (a). (c) GaAs-capped sample. (d) GPA of (c).

Strain at the QDs

These differences are shown in fig. 4.6. Figure 4.6b shows the strain map of a representative QD from the GaAs-capped sample. Figure 4.6d shows the strain map of a representative QD from the AlAs-capped sample. The biggest difference seems to be the magnitude of the strain. This is confirmed in fig. 4.7, which shows the strain in the AlAs-capped sample, where strain has a larger magnitude and is covering a larger area compared to the GaAs-capped sample.

4.1.3 Stacking faults

The quantum dot with stacking faults in the AlAs-capped sample has a very interesting feature: the strain from the QD itself has completly disappeared. This is shown in fig. 4.8. Figure 4.9 shows the averaged line plot over the dashed box in fig. 4.8b, and the averaged line plot of a wetting layer in same sample for comparison. Lastly fig. 4.10 show an LAADF-STEM image of the same QD, with extrapolation of the stacking faults to localize their origin.

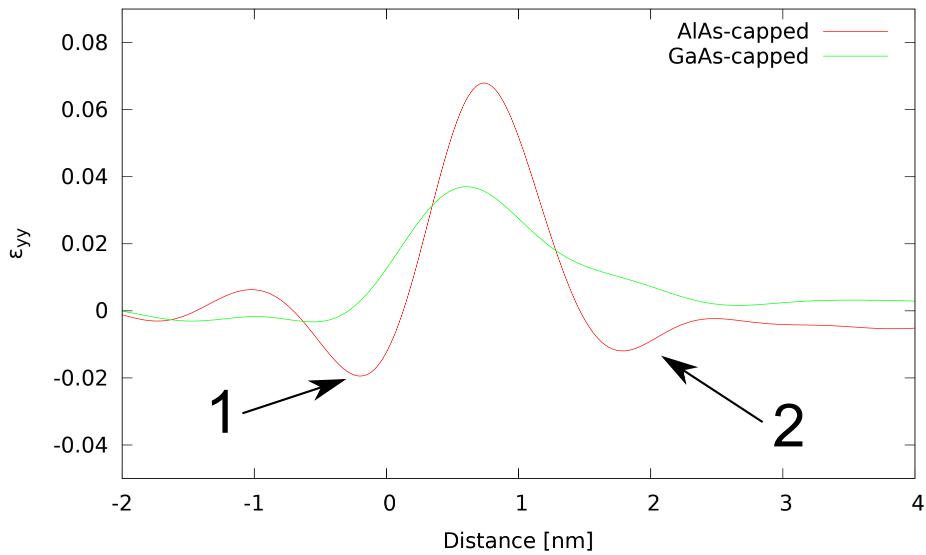

Figure 4.4: Averaged vertical line plots over the strain maps in fig. 4.3. The line plot is averaged over the whole map. AlAs-capped is from fig. 4.3b. GaAs-capped is from fig. 4.3d. (1) indicates negative strain right before the wetting layer. (2) indicates negative strain right after the wetting layer.

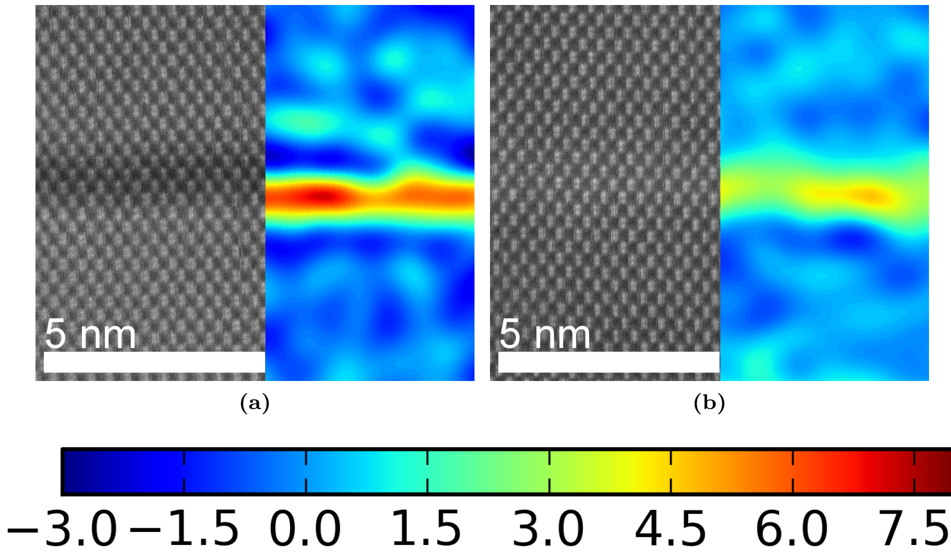

Figure 4.5: Composite of the images in fig. 4.3 showing the location of the strain. (a) Composite of the HAADF-STEM image fig. 4.3a and ε_{yy} strain map of the HAADF-STEM image fig. 4.3b. (b) Similar to (a) but composite of figs. 4.3c and 4.3d. Spatial resolution: 0.978 nm.

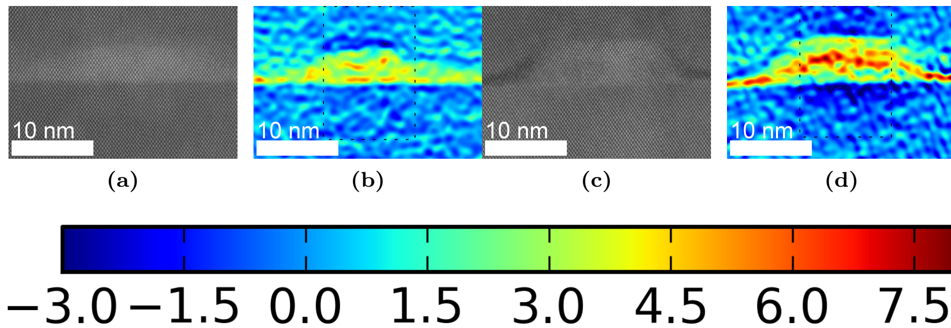

Figure 4.6: HAADF-STEM images and ε_{yy} strain maps of those images. Spatial resolution: 0.978 nm on all strain images. The dashed boxes in (b) and (d) show the area used for line plots in fig. 4.7. (a) HAADF-STEM image of the GaAs-capped sample. (b) Strain map of (a) in the ε_{yy} direction. (c) HAADF-STEM image of QD 2 in the AlAs-capped sample. (d) Strain map of (c) in the ε_{yy} direction.

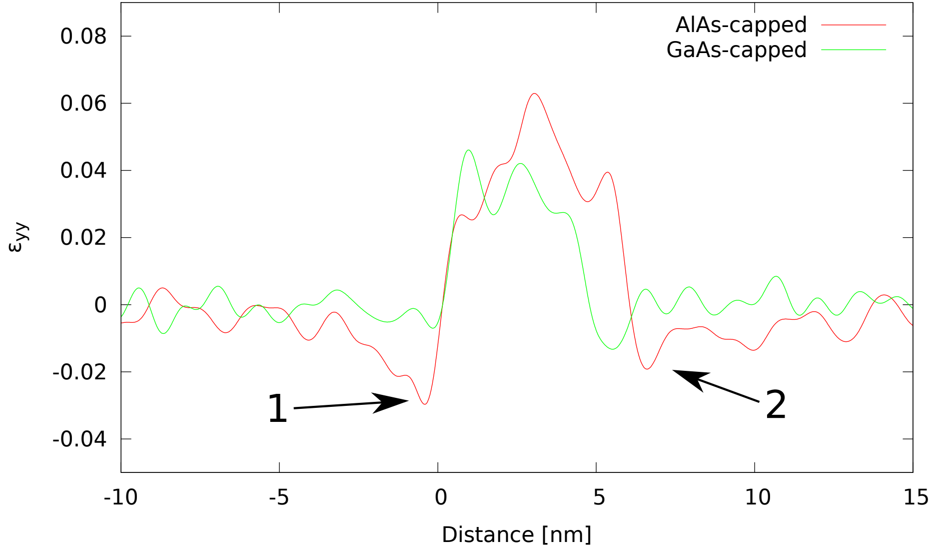

Figure 4.7: Averaged vertical line plots over strain maps in fig. 4.6. The dashed boxes shows the averaged area in each strain map. AlAs-capped is from fig. 4.6d. GaAs-capped is from fig. 4.6b.

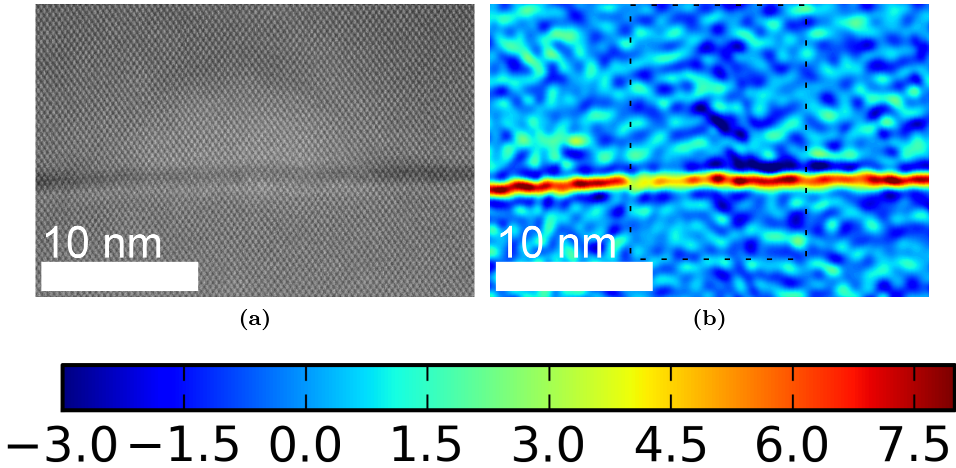

Figure 4.8: (a) HAADF-STEM image of QD 5, the one with stacking faults. (b) ε_{yy} strain map of (a). Spatial resolution: 0.978 nm. The dashed box shows the area used for line the plot in fig. 4.9.

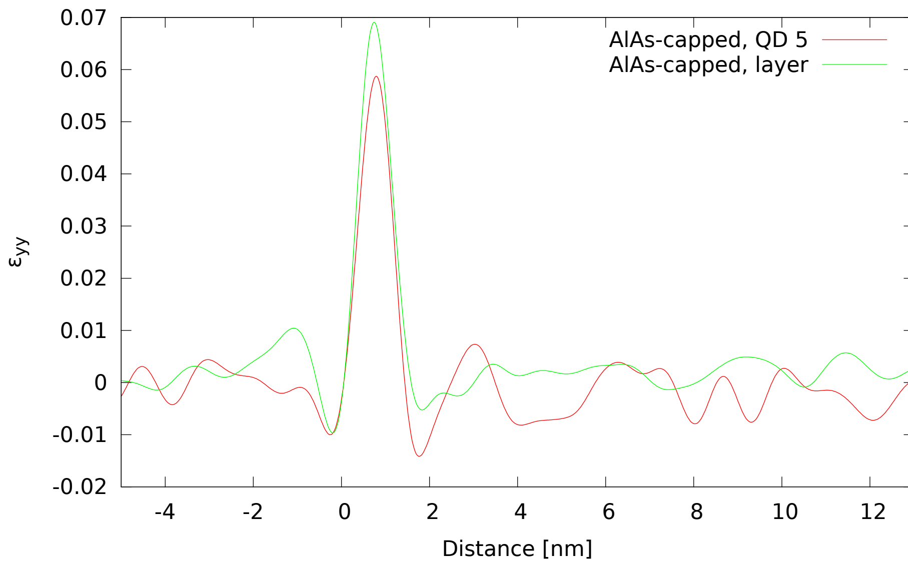

Figure 4.9: Averaged vertical line plot over the QD shown in fig. 4.8b. The dashed box in fig. 4.8b shows the averaged area. The line plot of the wetting layer is included for comparison.

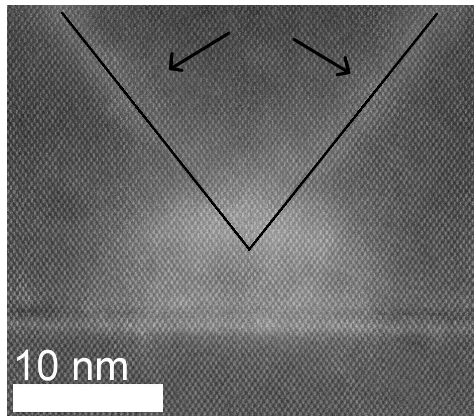

Figure 4.10: LAADF-STEM image showing stacking faults originating from the QD in fig. 4.8a. The black lines show an extrapolation of the stacking faults into the QD.

4.1.4 Reciprocal-space analysis

Another way of quantitatively analysing the strain is by looking at the power spectrumof the HRTEM images. The Bragg reflections parallel to the strain should be split or elongated. This is clearly the case in fig. 4.11c and 4.11d. The Bragg reflections are elongated towards the ⟨220⟩ axis, parallel to the growth direction. There does not appear to be any significant elongation parallel to the ⟨220⟩ direction. This implies little or no strain perpendicular to the growth direction. This corroborates the data from section 4.1.1.

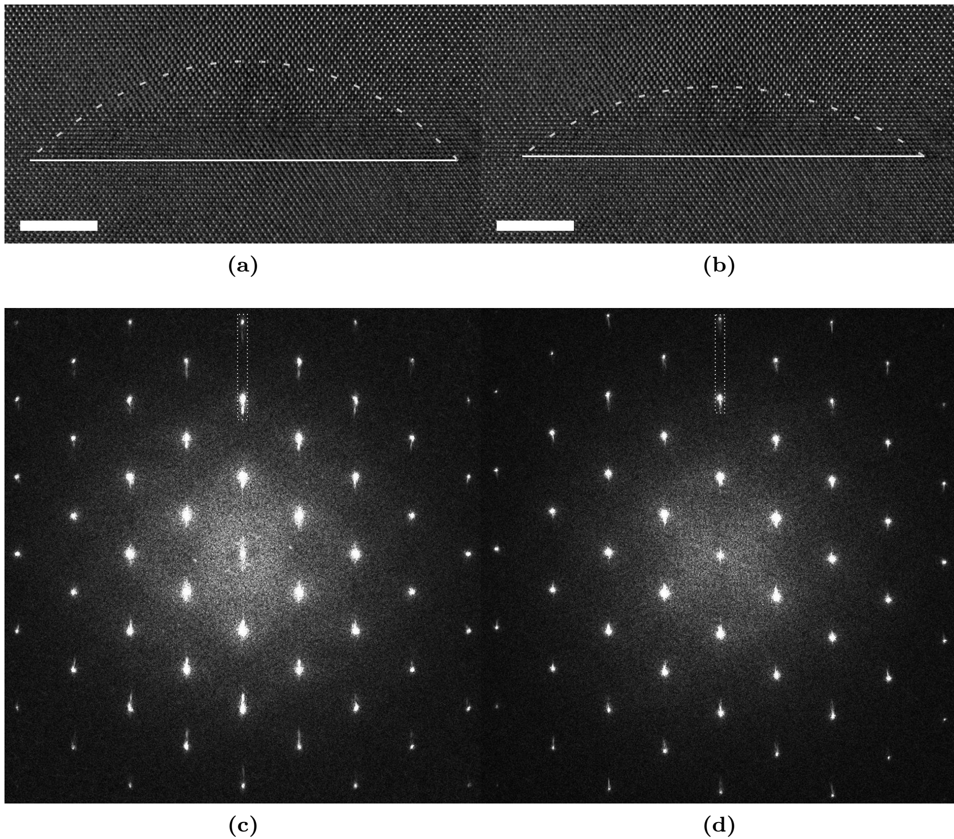

(a) **(b)** **(c)** **(d)**

Figure 4.11: (a) HRTEM of QD in the AlGa-capped sample. The solid line shows the wetting layer, dashed line showing the top of the QD. (b) Similar to (a) but from the GaAs-capped sample. (c) Power spectrum of the HRTEM image in (a). The dashed box is showing location of line plot used in fig. 4.12. (d) Similar to (c), but for the HRTEM image in (b).

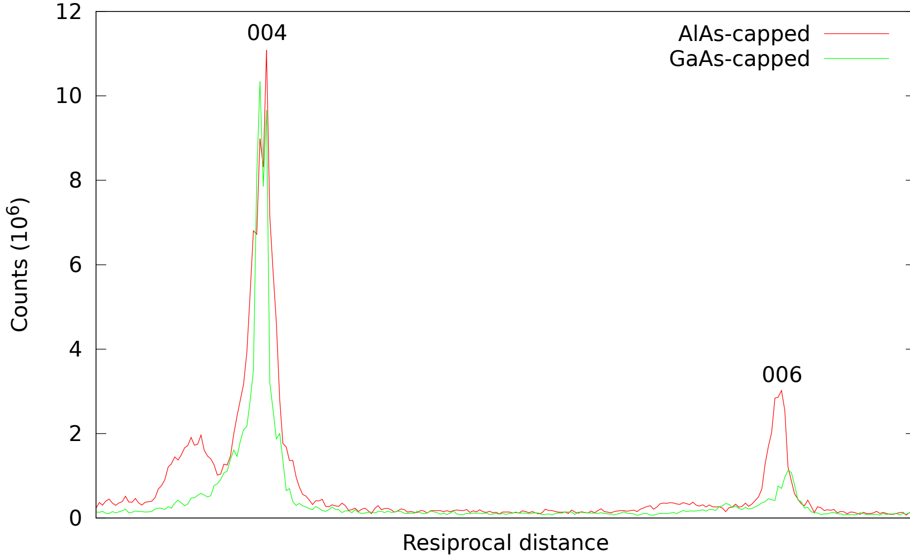

Figure 4.12: Averaged line plot of over the dashed boxes in fig. 4.11c (red) and fig. 4.11d (green) showing the elongation of the {004} and {006} Bragg reflections.

4.2 Multislice simulations

In this section and section 5.2 indium concentration, InAs-concentration and In-concentration will refer to the same thing. The results of the multislice simulations consists of intensity distributions of dumbbells as shown in fig. 4.13a where the simulated material was varied from 100% GaAs/0% InAs to 0% GaAs/100% InAs. Another variable was the thickness (z-direction) which varied from 0.1998 nm to 26 nm, with a step size of one unit cell in the z-direction (0.1998 nm). In addition every simulated dumbbell was averaged over 32 atomic/phonon configuration. All possible permutations of these two variables, thickness and In-concentration, were simulated. Then the average value for each dumbbell was calculated, and plotted in fig. 4.13b. This figure shows two expected features: the averaged intensity increases with thickness and indium concentration.

EELS data was used to calculate thickness an area of the sample with known composition. These reference areas were about 3 nm below the QDs, and are shown by black box in fig. 4.14a. Using eq. (3.1) the normalized intensity is calculated. The value $I_{\text{exp.mean}}$ was calculated by taking the mean intensity over the areas measured with EELS. The size of these areas were five dumbbells in both the x- and y-direction. The $I_{\text{exp.mean}}$ value was found using fig. 4.13b. The “blackcurrent” value $I_{\text{blackcurrent}}$ was retrived from a part of the sample where all the material had been sputtered away. Such an area is shown in fig. 3.4, between the arrows. By knowing the thickness and composition of the reference areas one could easily find

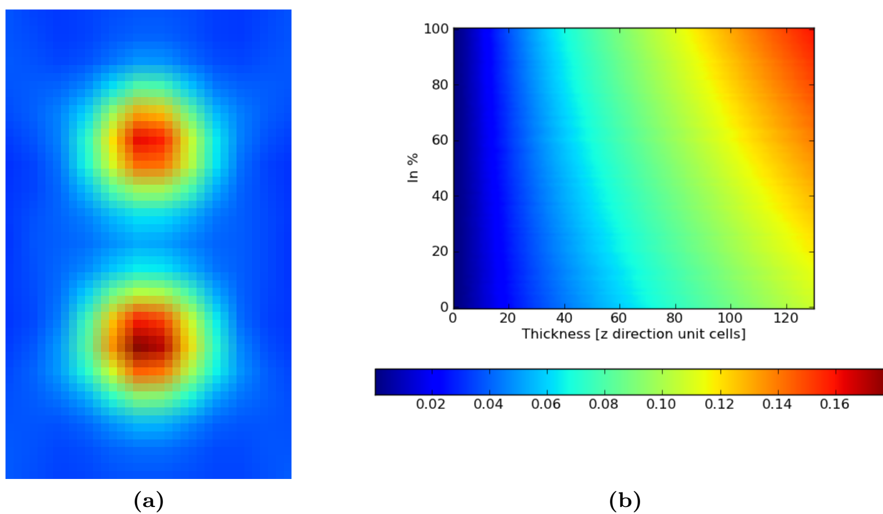

(a) **(b)**

Figure 4.13: (a) One simulated dumbbell where the simulated material was 100% GaAs, 20 nm and averaged over 32 atomic configurations. Similar dumbbells as shown in (a) was simulated for all InAs concentrations between 0 and 100% and for all thickness between 0.1998 nm to 26 nm. This result is shown in (b), where the simulated dumbbells have been averaged to one value and plotted as a function of the thickness and the indium concentration.

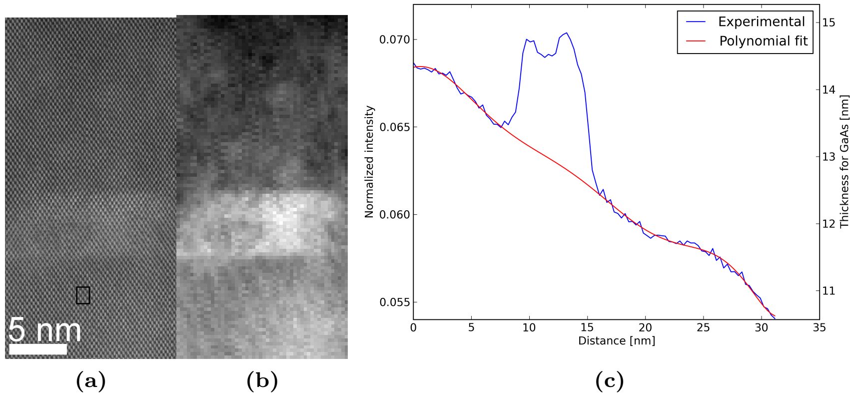

Figure 4.14: (a) HAADF-STEM image of QD 2 in the AlAs-capped sample. The black box shows the position where the EELS measurements were performed. (b) A pixelated version of (a), where areas consisting of 16 by 16 pixels have been merged. (c) The blue line shows the averaged line plot over (b). The red line shows an eight order polynomial fit over the blue line, except for the area from 6 to 19 nm. The left y-axis shows the normalized intensity calculated from eq. (3.1), while the right y-axis shows the corresponding thickness for 100% GaAs.

the corresponding simulated intensity. This enables the calculation of the thickness for the whole image.

After the normalization, the image is pixelated by combining 16 times 16 areas of pixels. This is done because of time constraints. Ideally one would analyze each atom-column, however that is a very time-consuming process. Calculating the chemical composition is a much faster process easier if the atom columns are averaged, as shown in fig. 4.14b.

Next the thickness plot is calculated from the pixelated image. The thickness was assumed to be approximately constant in the horizontal direction. Therefore the thickness in the vertical direction was calculated with a vertically averaged line plot over fig. 4.14b. This line plot is shown with the blue line in fig. 4.14c. The area between 0 nm to 6 nm and 19 nm to 31 nm in fig. 4.14c were assumed to be 100% GaAs. The area between 6 to 19 nm had an unknown chemical composition. A thickness estimation was calculated by removing this area, and doing an eight order polynomial fit on the remaining data (which consisted of GaAs). This polynomial fit is shown with the red line in fig. 4.14c.

Last the thickness distribution in fig. 4.14c, the thickness-composition plot in fig. 4.13b, and the pixelated image in fig. 4.14b is combined to get the indium distribution. This is most conviently explained with an example: the top-left pixel in fig. 4.14b has a thickness of about 10.5 nm (from the red plot in fig. 4.14c). The thickness gives one of the axes in the thickness-composition plot, and the intensity value of that pixel gives the other. The end result is the indium composition for

that pixel. This process is then repeated for all the pixels in the image. The indium composition for three different QDs calculated in this fashion is shown in fig. 4.15.

A line plot over the whole of figs. 4.15b to 4.15b is shown in fig. 4.16.

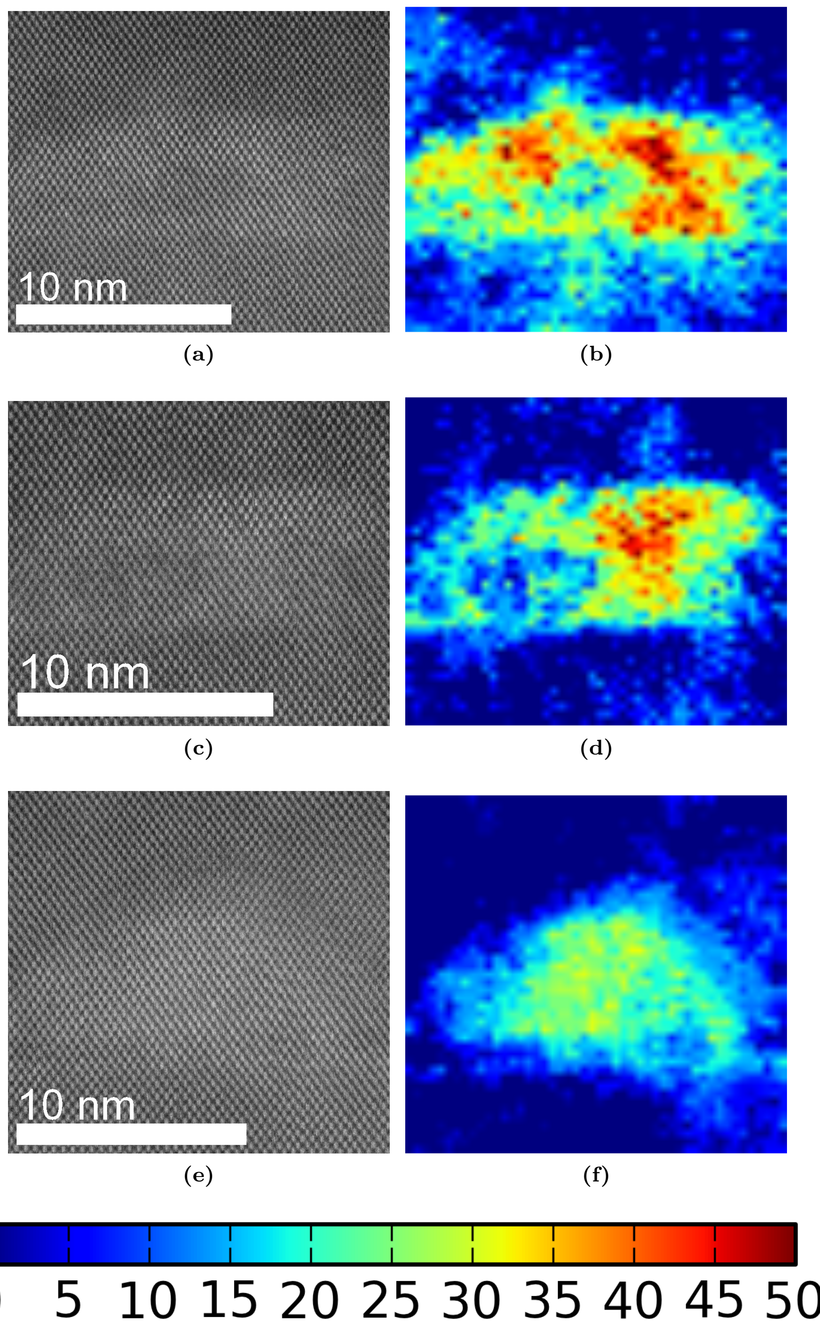

Figure 4.15: (a) HAADF-STEM image of the AlAs-capped sample. The thickness right below the QD was measured to be 14.5 nm. (b) Mapping of the Indium content in (a). (c) Similar as (a) except a measured thickness of 14.35 nm. (d) Mapping of the Indium content in (c).(e) Similar as (a) except a measured thickness of 23.10 nm. (f) Mapping of the Indium content in (e).

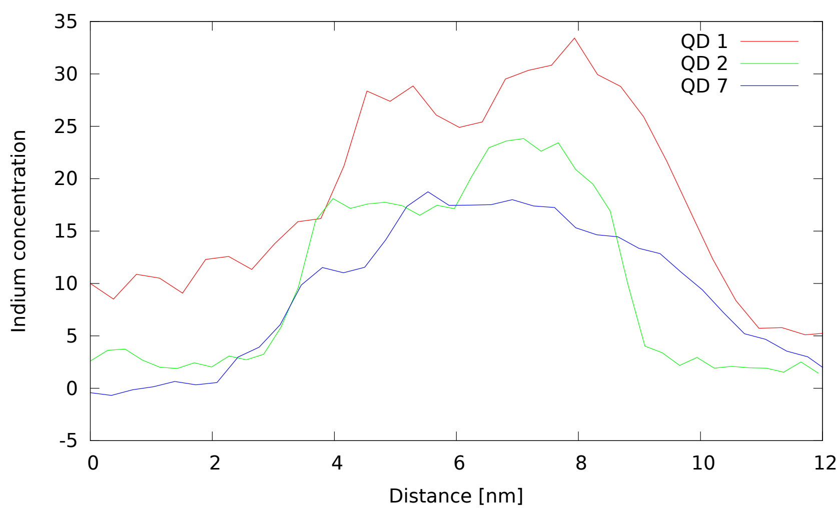

Figure 4.16: Averaged vertical line plots over the indium concentration maps shown in fig. 4.15.

Chapter 5

Discussion

The discussion is divided into three parts. First I discuss the strain analysis, where the results from the GPA and reciprocal-space analysis will be discussed. Then the multislice simulation part, where the comparison between the experimental STEM and multislice simulations will be discussed.

5.1 Strain analysis

5.1.1 Strain direction

The data in sections 4.1.1 and 4.1.4 indicate negligible strain in the ε_{xx} direction. This is a result of how the sample was grown, as explained in section 2.2.1. The material was grown slowly, layer by layer. Both GaAs and InAs have the zinkblende structure, and the most energitically favorable situation is to retain this structure. When InAs is deposited on GaAs it wants to retain the size of its unit cell, which is larger than that of GaAs's. The InAs wants to expand somewhere to minimize the compression of its unit cell. The only free direction is the growth direction which is parallel to ε_{yy}. Expanding in the ε_{xx} direction would require shifting the underlying lattice. This would be less energetically favorable.

A few STEM images with the scan direction parallel to the ε_{xx} could have yielded more information on the strain in this direction. Unfortunately such images were not taken during the TEM session in Denmark..

5.1.2 GaAs-capped vs. AlAs-capped

Starting with the wetting layers in figs. 4.3 and 4.4, one notices several interesting features. The most prominent feature is the difference in strain magnitude. This is clearly shown in the plot in fig. 4.4. The wetting layer in the AlAs-capped sample peaks at about 7% strain. The wetting layer in the GaAs-capped sample peaks at about 4% strain. The calculations in section 2.2.1 gave a strain of 19% in the y-direction with pure InAs on a GaAs substrate. This indicate no monolayers being 100% InAs. That means there is a mix of InAs, GaAs and AlAs instead of pure

InAs. One important thing to keep in mind, is the different amounts of InAs in the two samples. The AlAs-capped sample was grown with 2.8 monolayers of InAs. The GaAs-capped sample was grown with 2.3 monolayers of InAs. This will reduce the amount of strain in the GaAs-capped sample.

Figure 4.4 indicates that the indium is distributed differently in the two samples. The wetting layer in the AlAs-capped sample has a higher and narrower peak than the wetting layer in the GaAs-capped sample. One factor could be the higher growth temperature (500 vs. 512 °C), but the major factor is probably the AlAs-capping. The AlAs-capping is thought to reduce the diffusion length of the indium[42]. This effect would reduce the amount of indium diffusing into the layer above.

The position of the InAs can be inferred in fig. 4.5. For the AlAs-capped sample the strain is concentrated right on the border of the darker region. This leads credence to the hypothesis of the AlAs-capping preventing the diffusion of the indium. The opposite is seen in fig. 4.5b, where the strain is spread over a larger area. This imples the indium has diffused into the GaAs-capping, at least to a larger degree than in the AlAs-capped sample.

The quantum dots in fig. 4.6 show similar patterns as the layers examined earlier: QDs in the GaAs-capped sample have less amount of strain, than the QDs in the AlAs-capped sample. Figure 4.7 show the strain in the QD in the AlAs-capped sample peak at about 6% strain. The strain in the GaAs-capped QD peak at about 4%. One difference is the apparent size of the strained area. The area with positive strain is larger in the AlAs-capped sample. Arrows (1) and (2) in fig. 4.7 show an additional feature: an area with negative strain, both above and below the AlAs-capped QD. The feature is also present above the GaAs-capped QD, but seem to be smaller in magnitude. This effect is probably caused by compression of GaAs, and is explained by looking at a larger part of the system. Most of the sample volum between the wetting layers is GaAs. The QDs expand the lattice locally, however the lattice should return back to GaAs's lattice parameters. This process is often called strain relaxation. In fig. 4.6d the system is returned to GaAs bulk parameters by compressing the lattice in the growth direction both above and below the QD.

Figure 4.12 confirm the findings of less amount of strain in the GaAs-capped sample. The AlAs-capped peaks (red) are split to a larger degree than the GaAs-capped peaks (green). This implies greater amounts of straining in the AlAs-capped sample.

5.1.3 Strain relaxation through stacking fault

The most interesting result is found in the quantum dot with stacking faults in the AlAs-capped sample. The strain map in fig. 4.8b is almost identical to that strain map of the wetting layer in fig. 4.3b. This implies all the strain in the QD has been relaxed through the stacking faults. The occurance of stacking faults imply a large degree of strain inside the QD. A large degree of strain implies a large amount of InAs, implying this is a larger QD than the others[48]. Finding the exact origin of the stacking fault inside the QD would be valuable. This information could give an

indication on where the most InAs is located. Figure 4.10 show an extrapolation of the stacking faults. The stacking faults seem to originate from the top-half of the QD, indicating the location of the most InAs. Gerthsen et al.[49] investigated a similar system, and found the largest concentration of InAs towards the top of QD.

5.2 Multislice simulations

A value for the error can be derived from fig. A.1. The areas far away from the QD should consist of pure GaAs and these areas should show an indium content of 0% on fig. A.1b. The largest error seems to be to the left part on the map, marked by the arrows 1 and 2. These deviations are probably caused by horizontal thickness variations. The thickness was assumed to be constant in the horizontal direction because of time constraints. However this assumption will introduce errors as seen in fig. A.1b. Luckily the thickness gradient was mostly in the vertical direction for the analysed QDs. This problem is solved by creating a two-dimensional thickness map, instead of the one-dimensional thickness-curve used here. Based on fig. A.1b this errorbars are estimated to be about $\pm$ 10%.

Another source of error is strain. As explained in section 2.4.6, strain will effect the intensity in HAADF images. This will probably be strongest at the QDs, because of their non-uniform strain field. However even the fairly uniform strain at the wetting layers will be effected by this, because of surface relaxations[36]. The surface relaxation effect will probably effect the QDs at the thinnest areas the most, because they are more likely to have parts of their strained surface exposed to the vacuum. These effects will probably lead to a decrease in the estimated amount indium. It is possible to correct for the strain effects at QDs. One way is the simulate the whole quantum dot. However this would be very complicated, since the strain inside the QD would have to be calculated somehow as well. Parts of this has been done by using GPA, but this will only yield a projection of the three-dimensional strain field. The nature of the strain field along the surface of the QD is unknown and would require some different technique.

The AlAs-capping also effects the estimation of the indium concentration. AlAs will give less contrast than GaAs or InAs, because alumininum has a smaller atomic number. This effect is clearly seen at the wetting layer in fig. 4.8. This effect will be strongest in QDs at thick areas, because of less amount of the wetting layer having been removed. The effect from the wetting layer is probably minimal in QD 1 and 2, because the sample is about 14 nm thick at that area and the width of QD 1 and 2 is about 15 nm. The shape of the QDs is close to being symmetrical in the growth plane[50]. In addition the AlAs-cap will be laying on top the QDs as shell, lowering the intensity from the QD.

Figure 4.15 shows indium concentration maps from three different QDs in the AlAs-capped sample. The biggest qualitatitive difference is the lower indium concentration in QD 7 in fig. 4.15f. This is caused by the QD being in a thicker area, reducing the relative amount of InAs in the area. The location of QD 1 and 2 is therefore more preferable for calculating the indium concentration. Figure 4.16

shows the averaged indium content in QD 1, 2 and 7. This indicates an average indium concentration in QD 1 from about 20-30%, with peaks up to 50%. The indium in QD 2 seems to have a different form. This is probably caused by parts of the QD being removed in the sample preparation process. This probably means the less indium remains in the QD. QD 2 has an average indium concentration of about 20%, and a peak at about 50% indium. Both these estimates are probably too low, caused by the error sources described earlier.

Chapter 6

Conclusion

This thesis has explored the strain properties of two InAs/GaAs quantum dot intermediate band solar cell materials. One sample had an AlAs-cap, while the other had a GaAs-cap. By using GPA the strain in the quantum dots and the wetting layer was examined. Several differences were observed. Strain in the wetting layer in the AlAs-capped sample had a larger magnitude compared to the GaAs-sample, and was confined to a smaller area. The strain in the quantum dots in the AlAs-capped sample had a larger magnitude compared to the GaAs-capped sample, and covered a larger area. Features which were observed in both the samples, but were larger in the AlAs-capped sample. Negative strain right below and above the quantum dots and wetting layer. No strain perpendicular to the growth direction.

In addition the chemical composition of the quantum dots in the AlAs-capped sample was estimated. This was done by using HAADF-STEM and multislice simulations. The experimental data was normalized by using a part of the sample with known chemical composition. Then the data was compared to multislice simulations. The average indium concentration in the quantum dots were averaged to 20-30% $\pm$ 10%, with peaks up to 50%. These estimates were probably low estimates because of two effects: dechanneling, and aluminum reducing the HAADF-STEM signal.

Chapter 7

Further work

There are several further courses of inquiry.

Further strain analysis on the existing data could yield more information about the indium content inside the wetting layer.

Analysis of individual atom columns could yield higher accuracy with regards to estimating the indium concentration. Calculating the exact amount of strain which is relaxed due to the stacking fault in quantum dot 5. This could yield information about the threshold for the formation of stacking faults.

References

[1] http://www.eia.doe.gov/oiaf/ieo/world.html. Accessed 9/12/2010.

[2] http://www.wfs.org/futintervja07.htm. Accessed 13/12/2010.

[3] Hermann WA. *Quantifying global exergy resources. Energy*, 31(12):1685 – 1702, 2006. ISSN 0360-5442. doi:DOI:10.1016/j.energy.2005.09.006.

[4] Martí A and Araújo GL. *Limiting efficiencies for photovoltaic energy conversion in multigap systems. Solar Energy Materials and Solar Cells*, 43(2):203 – 222, 1996. ISSN 0927-0248. doi:DOI:10.1016/0927-0248(96)00015-3.

[5] Shockley W and Queisser HJ. *Detailed balance limit of efficiency of p-n junction solar cells. Journal of Applied Physics*, 32(3):510–519, 1961. doi:10.1063/1.1736034.

[6] Green MA. *Third generation photovoltaics: solar cells for 2020 and beyond. Physica E: Low-dimensional Systems and Nanostructures*, 14(1-2):65 – 70, 2002. ISSN 1386-9477. doi:DOI:10.1016/S1386-9477(02)00361-2.

[7] http://en.wikipedia.org/wiki/File:Scheme_TEM_en.svg. Accessed 13/12/2010.

[8] Martí A, Antolín E, Stanley CR, Farmer CD, López N, Díaz P, Cánovas E, Linares PG, and Luque A. *Production of photocurrent due to intermediate-to-conduction-band transitions: A demonstration of a key operating principle of the intermediate-band solar cell. Phys. Rev. Lett.*, 97(24):247701, 2006. doi:10.1103/PhysRevLett.97.247701.

[9] Wolf M, Brendel R, Werner JH, and Queisser HJ. *Solar cell efficiency and carrier multiplication in Si(1-x)Ge(x) alloys. Journal of Applied Physics*, 83(8):4213–4221, 1998. doi:10.1063/1.367177.

[10] Ellingson RJ, Beard MC, Johnson JC, Yu P, Micic OI, Nozik AJ, Shabaev A, and Efros AL. *Highly Efficient Multiple Exciton Generation in Colloidal*

PbSe and PbS Quantum Dots. Nano Letters, 5(5):865–871, 2005. doi:10.1021/nl0502672.

[11] Hanna MC and Nozik AJ. *Solar conversion efficiency of photovoltaic and photoelectrolysis cells with carrier multiplication absorbers. Journal of Applied Physics*, 100(7):074510, 2006. doi:10.1063/1.2356795.

[12] Martí A, López N, Antolín E, Cánovas E, Stanley C, Farmer C, Cuadra L, and Luque A. *Novel semiconductor solar cell structures: The quantum dot intermediate band solar cell. Thin Solid Films*, 511-512:638 – 644, 2006. ISSN 0040-6090. doi:DOI:10.1016/j.tsf.2005.12.122. EMSR 2005 - Proceedings of Symposium F on Thin Film and Nanostructured Materials for Photovoltaics - EMRS 2005- Symposium F.

[13] Conibeer G. *Third-generation photovoltaics. Materials Today*, 10(11):42 – 50, 2007. ISSN 1369-7021. doi:DOI:10.1016/S1369-7021(07)70278-X.

[14] Marti A, Cuadra L, and Luque A. *Quantum dot intermediate band solar cell.* In *Photovoltaic Specialists Conference, 2000. Conference Record of the Twenty-Eighth IEEE*, pages 940 –943. 2000. doi:10.1109/PVSC.2000.916039.

[15] Reed MA, Randall JN, Aggarwal RJ, Matyi RJ, Moore TM, and Wetsel AE. *Observation of discrete electronic states in a zero-dimensional semiconductor nanostructure. Phys. Rev. Lett.*, 60(6):535–537, 1988. doi:10.1103/PhysRevLett.60.535.

[16] Smestad GP. *Optoelectronics of Solar Cells.* SPIE Press, United States of America, 2002.

[17] Luque A, Martí A, López N, Antolín E, Cánovas E, Stanley C, Farmer C, Caballero LJ, Cuadra L, and Balenzategui JL. *Experimental analysis of the quasi-Fermi level split in quantum dot intermediate-band solar cells. Applied Physics Letters*, 87(8):083505, 2005. doi:10.1063/1.2034090.

[18] Würfel P. *Limiting efficiency for solar cells with defects from a three-level model. Solar Energy Materials and Solar Cells*, 29(4):403 – 413, 1993. ISSN 0927-0248. doi:DOI:10.1016/0927-0248(93)90099-O.

[19] Martí A, Cuadra L, and Luque A. *Design constraints of the quantum-dot intermediate band solar cell. Physica E: Low-dimensional Systems and Nanostructures*, 14(1-2):150 – 157, 2002. ISSN 1386-9477. doi:DOI:10.1016/S1386-9477(02)00368-5.

[20] Cuadra L, Martí A, and Luque A. *Present status of intermediate band solar cell research. Thin Solid Films*, 451-452:593 – 599, 2004. ISSN 0040-6090. doi:DOI:10.1016/j.tsf.2003.11.047. Proceedings of Symposium D on Thin Film and Nano-Structured Materials for Photovoltaics, of the E-MRS 2003 Spring Conference.

[21] GF Brown JW. *Third generation photovoltaics. Laser & Photonics Review*, 2009. doi:10.1002/lpor.200810039.

[22] Popescu V, Bester G, Hanna MC, Norman AG, and Zunger A. *Theoretical and experimental examination of the intermediate-band concept for strain-balanced (In,Ga)As/Ga(As,P) quantum dot solar cells. Phys. Rev. B*, 78(20):205321, 2008. doi:10.1103/PhysRevB.78.205321.

[23] Luque A and Martí A. *The intermediate band solar cell: Progress toward the realization of an attractive concept. Advanced Materials*, 22(2):160–174, 2010. doi:10.1002/adma.200902388.

[24] Albert G Baca CIHA. *Fabrication of GaAs Devices.* Institution of Engineering and Technology, 2005.

[25] Kurtz SR, Faine P, and Olson JM. *Modeling of two-junction, series-connected tandem solar cells using top-cell thickness as an adjustable parameter. Journal of Applied Physics*, 68(4):1890 –1895, 1990. ISSN 0021-8979. doi:10.1063/1.347177.

[26] Adachi S. *GaAs and Related Materials.* World Scientific, Singapore, 1999.

[27] Krier A and Sherstnev VV. *Powerful interface light emitting diodes for methane gas detection. Journal of Physics D: Applied Physics*, 33(2):101, 2000.

[28] J S. *Physics of semiconductors and their heterostructures.* McGraw-Hill, USA, 1993.

[29] Smith DL. *Thin-film deposition.* McGraw-Hill, United States of America, 1995.

[30] Thomassen SF, Reenaas TW, and Fimland BO. *InAs/GaAs quantum dot density variation across a quarter wafer when grown with substrate rotation. Journal of Crystal Growth*, 2010. In press.

[31] Marian A Herman HS. *Molecular Beam Epitaxy.* Springer, Berlin Heidelberg, 1996.

[32] Zhuang Q, Li H, Pan L, Li J, Kong M, and Lin L. *Self-organization of the InGaAs/GaAs quantum dots superlattice. Journal of Crystal Growth*, 201-202:1161 – 1163, 1999. ISSN 0022-0248. doi:DOI:10.1016/S0022-0248(99)00010-X.

[33] David B Williams CBC. *Transmission Electron Microscopy.* Springer, United States of America, 2009.

[34] Luque A and Martí A. *Increasing the efficiency of ideal solar cells by photon induced transitions at intermediate levels. Phys. Rev. Lett.*, 78(26):5014–5017, 1997. doi:10.1103/PhysRevLett.78.5014.

[35] Batson PE, Dellby N, and Krivanek OL. *Sub-angstrom resolution using aberration corrected electron optics.* *Nature*, 418:617–620, 2002. doi:10.1038/nature00972.

[36] Grillo V. *The effect of surface strain relaxation on haadf imaging.* *Ultramicroscopy*, 109(12):1453 – 1464, 2009. ISSN 0304-3991. doi:DOI:10.1016/j.ultramic.2009.07.010.

[37] Erni R. *Aberration-Corrected Imaging in Transmission Electron Microscopy.* Imperial Collage Press, Singapore, 2010.

[38] Brandon D and Kaplan WD. *Microstructual Characterization of Materials.* John Wiley & Sons Ltd, Great Britain, 2008.

[39] Egerton R. *Electron Energy-Loss Spectroscopy in the Electron Microscope.* Plenum Press, USA, 1996.

[40] Kirkland EJ. *Advanced Computing in Electron Microscopy.* Springer, USA, 2010.

[41] Bransden B and Joachain C. *Quantum Mechanics.* Pearson Education, Malaysia, 2000.

[42] Andrews A, Schramboeck M, Roch T, Schrenk W, Gornik E, and Strasser G. *Independent control of InAs quantum dot density and size on AlxGa(1–x)As surfaces.* *Journal of Materials Science: Materials in Electronics*, 19:714–719, 2008. ISSN 0957-4522. 10.1007/s10854-007-9389-z.

[43] `http://www.microscopy.cen.dtu.dk/microscopes/Titan/ATEMspecs.html`. Accessed 20/06/2011.

[44] `http://www.microscopy.cen.dtu.dk/microscopes/Titan/ETEMspecs.html`. Accessed 20/06/2011.

[45] Sanchez AM, Galindo PL, Kret S, Falke M, Beanland R, and Goodhew PJ. *Quantitative strain mapping applied to aberration-corrected haadf images.* *Microscopy and Microanalysis*, 12(04):285–294, 2006. doi:10.1017/S1431927606060363.

[46] Chung J, Lian G, and Rabenberg L. *Practical and reproducible mapping of strains in si devices using geometric phase analysis of annular dark-field images from scanning transmission electron microscopy.* *Electron Device Letters, IEEE*, 31(8):854 –856, 2010. doi:10.1109/LED.2010.2049562.

[47] Schowalter M, Rosenauer A, Titantah JT, and Lamoen D. *Computation and parametrization of the temperature dependence of Debye–Waller factors for group IV, III–V and II–VI semiconductors.* *Acta Crystallographica Section A*, 65(1):5–17, 2009. doi:10.1107/S0108767308031437.

[48] Frigeri P, Nasi L, Prezioso M, Seravalli L, Trevisi G, Gombia E, Mosca R, Germini F, Bocchi C, and Franchi S. *Effects of the quantum dot ripening in high-coverage inas/gaas nanostructures. Journal of Applied Physics*, 102(8):083506, 2007. doi:10.1063/1.2795661.

[49] Rose HH. *Optics of high-performance electron microscopes. Science and Technology of Advanced Materials*, 9(1):014107, 2008.

[50] Inoue T, Kita T, Wada O, Konno M, Yaguchi T, and Kamino T. *Electron tomography of embedded semiconductor quantum dot. Applied Physics Letters*, 92(3):031902, 2008. doi:10.1063/1.2837453.

Appendix A

Indium concentration, error estimate

Figure A.1b shows a large area where the indium composition has been calculated. The areas at the top and bottom parts of the map should be 100% GaAs, and should show 0% indium. This is used to estimate the error in the indium composition maps

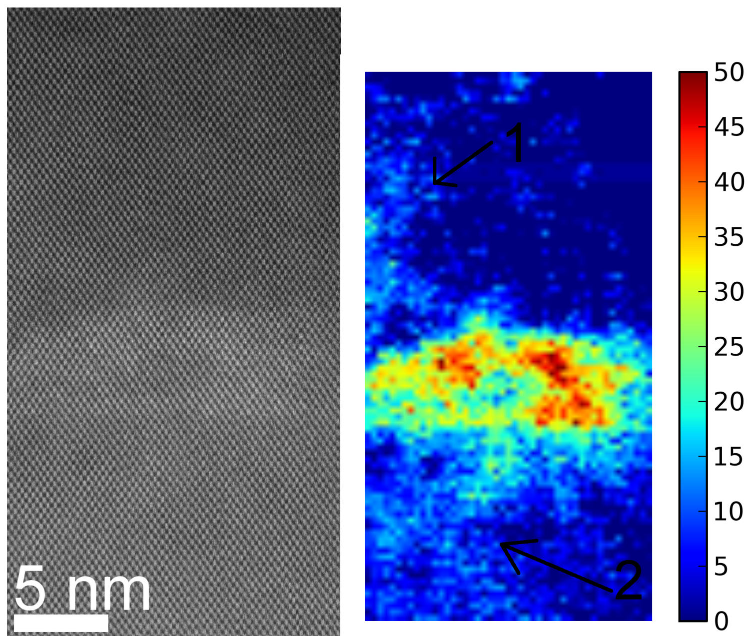

Figure A.1: (a) HAADF-STEM image of QD 1 in the AlAs-capped sample. (b) Map showing the indium content in (a). Arrow 1 is showing an area with high indium concentration above the QD. Arrow 2 showing the same, but below the QD.

.